



CHORUS

This is the accepted manuscript made available via CHORUS. The article has been published as:

Wake characteristics of a utility-scale wind turbine under coherent inflow structures and different operating conditions

Xiaolei Yang and Fotis Sotiropoulos

Phys. Rev. Fluids **4**, 024604 — Published 12 February 2019

DOI: [10.1103/PhysRevFluids.4.024604](https://doi.org/10.1103/PhysRevFluids.4.024604)

Wake characteristics of a utility-scale wind turbine under coherent inflow structures and different operating conditions

Xiaolei Yang

*Department of Civil Engineering, Department of Mechanical Engineering,
College of Engineering and Applied Sciences, Stony Brook University, Stony Brook, New York 11794, USA*

Fotis Sotiropoulos

*Department of Civil Engineering, College of Engineering and Applied Sciences,
Stony Brook University, Stony Brook, New York 11794, USA*

Understanding the wake characteristics of wind turbines under the influence of atmospheric turbulence is crucial for developing advanced turbine control algorithms, such as the coordinated turbine control for improving the performance of the entire wind farm as an integrated system. In this work, we systematically investigate the wake of a utility scale wind turbine for different thrust coefficients, which is relevant to the coordinated axial induction control. Large-eddy simulation (LES) with novel actuator surface models for turbine blades and nacelle is employed to simulate turbine wakes. Different thrust coefficients are achieved by varying the tip-speed ratio, i.e. $\lambda = 6.8, 7.8, 8.8, 9.3$. The inflow is generated from a precursory simulation using a very large computational domain to include the large-scale flow structures in atmospheric turbulence. The computed results show that varying the tip-speed ratio gives rise to differences in wake statistics, such as the wake recovery rate and the turbulence intensity. On the other hand, the computed results also reveal similarities in wakes from different tip-speed ratios. It is found that the characteristic velocity defined by the thrust on the rotor scales the turbine-added turbulence kinetic energy computed based on different wake center locations. For all considered tip-speed ratios, two dominant frequencies of the large-scale motion of the wake are observed, one is the dominant low frequency of the large-scale flow structures in the inflow prevailing at almost all downwind locations, the other one is the frequency of Strouhal number about 0.15 prevailing at far wake locations ($> 3 \sim 4$ rotor diameters). The existence of the inflow frequency in the large-scale motion of wakes shows the effects of incoming large-scale flow structures on wake meandering. The Strouhal number of the second frequency, on the other hand, is typical for that of vortex shedding behind bluff bodies. This finding suggests the coexistence of the two mechanisms for wake meandering, i.e. inflow large-scale turbulent flow structures and the wake shear layer instability, with the corresponding motion termed inflow-driven wake meandering and shear-induced wake meandering, respectively. The effects of wake and turbine energy extraction on motion of different frequencies are examined for different tip-speed ratios. As approaching the turbine upwind, the energy of the low frequency motion of the inflow is significantly attenuated, while the energy of the motion at frequencies higher than the inflow low frequency are observed to increase for most cases. In the near wake, decreases of energy are observed for all the frequencies in almost all the cases. At far wake locations, the energy of the motion at all frequencies is increased to a level higher than that of the inflow (at 2D turbine upwind) in almost all the cases. At last the statistics of wake centers in the spanwise and vertical directions are examined. It is found that the probability density function (PDF) profiles of wake center fluctuations nearly collapse with each other for different tip-speed ratios. The Gaussian distribution is found to be an acceptable approximation for the PDF of wake center locations at near wake locations (e.g. 2D, 4D and 6D turbine downwind), while it is a poor approximation at far wake locations (greater than 8D turbine downwind). Downwind variations of the mean values and the standard deviations of wake center fluctuations are also observed to nearly collapse with each other for different tip-speed ratios. The observed similarities of turbine wake statistics illuminate the possibility of developing advanced engineering models taking into account the unsteady features of turbine wakes for advanced turbine controls.

I. INTRODUCTION

The turbines in a wind farm are coupled with each other through turbine wakes and the interaction of turbine wakes with the atmospheric turbulence. The complexity of turbine wake dynamics in the atmospheric turbulent flow poses a great challenge for maximizing the performance of the entire wind farm as an integrated energy producing system using the advanced wind farm control strategies. There are several advanced wind farm control strategies existing in the literature, such as the coordinated turbine control through axial induction factor [1–3], the yaw-based and tilt-based wake redirection methods [3, 4], and the IPC (individual pitch control)-based methods [4]. To develop such advanced turbine control algorithms requests an improved understanding of turbine wake dynamics and its interaction with the atmospheric turbulence for different turbine operating conditions. The particular interest of this work is to investigate the wake dynamics of a utility-scale wind turbine under an inflow with large-scale coherent structures for different tip-speed ratios, which is relevant to the coordinated axial induction control.

Inflow conditions have significant effects on turbine wake dynamics. Some studies focused on uniform inflows, e.g. Troldborg et al. [5] investigated the wake of a wind turbine operating in a uniform inflow at various tip-speed ratios. The uniform inflow case can provide insights into wake dynamics, e.g. tip and hub vortices and their interactions, however, it cannot represent the wind with shear and atmospheric turbulence in the real world. Investigations of turbine wakes under more realistic incoming wind conditions, which take into account the effects of different ground roughness, thermal stratifications and terrain conditions, have been carried out in wind tunnel experiments [6]. For instances, Chamorro and Porté-Agel studied the wake of a model wind turbine placed on rough and smooth surfaces in [7], and the wake of the same model wind turbine under both neutral and stably stratified conditions in [8]. Zhang et al. [9] investigated the wake of a model wind turbine under convective boundary layer conditions. Investigations of turbine wakes under site-specific complex inflows were focused on simple terrain topography in wind tunnel experiments, e.g. Howard et al. [10] investigated the influences of the wake of a three-dimensional, sinusoidal hill on the wake of a model wind turbine. Chamorro et al. [11] investigated the effects of energetic coherent flow structures induced by upstream cylinders on the wake of an axial-flow hydrokinetic turbine. Wind tunnel experiments can provide valuable datasets for investigating the wake dynamics and validating computational models. However, the turbines employed in wind tunnel experiments are usually one to two orders of magnitude smaller than utility-scale wind turbines, which makes the findings of wind tunnel experiments not directly applicable to utility-scale wind turbines. Field-scale measurements [12–15] are very important for validating and verifying computational models and laboratory-scale experiments. However, the data obtained from field-scale measurements are usually constrained to certain locations and suffer from uncertainties from the environmental conditions and the turbine operating conditions. Compared with experiments in fields and laboratories, the advantage of high-fidelity computational models (e.g. LES) lies in their capability to provide high-resolution, three-dimensional wind fields in wakes of utility-scale turbines under well-controlled inflow, terrain and turbine operating conditions. The atmospheric realism of the inflow turbulent structures plays an important role on how well the LES predictions can represent the wake dynamics of utility-scale wind turbines in the real world. The synthetic turbulence technique is usually employed to generate the turbulence in the inflow, e.g. Yang et al. [16] investigated the effects of the synthetic turbulence on the LES of utility-scale wind turbines when using the wind field computed from the Weather Research and Forecasting model as the inflow. Specific levels of turbulence intensity can be achieved using the synthetic turbulence technique. However, the generated large-scale flow structures are in general not realistic. More realistic turbulence in the inflow can be generated from a precursory simulation. Recently, a technique using spires at the inlet to generate energetic coherent structures in the inflow was developed by Foti et al. [17]. In the precursory simulation for inflows, the domain size of the precursory simulation is usually the same or comparable with that employed in the turbine simulation. The large-scale atmospheric turbulence can be captured in simulations of large wind farms because of the employed large computational domain. Such structures cannot be captured, however, in a small domain simulation of an individual turbine if the same domain size is employed in the precursory inflow simulation.

Nacelle induced coherent structures were shown to have a significant impact on turbine wake characteristics, such as velocity deficits, turbulence intensities and wake meandering [18–21]. It was shown in [22] that the actuator line model without a nacelle model cannot accurately capture the wake meandering of a hydrokinetic turbine, and underpredicts the turbulence intensity at far wake locations. Santoni et al. [23] also found the effects of nacelle on the velocity deficits and turbulence intensity for the “Blind test 1” turbine at the Norwegian University of Science and Technology and proposed to use the immersed boundary method for modeling the turbine nacelle [24]. The nacelle can be represented by a permeable disk with a specified drag coefficient, which however cannot take into account the nacelle effect accurately as shown in [16, 25]. In [25] an actuator surface model for nacelle was proposed, which can capture the nacelle wake dynamics and its effect on far wake meandering on coarse meshes typical to those used in actuator disk/line simulations. In this work, we employ LES with the actuator surface models for turbine blades and nacelle [25] for simulating the turbine wakes.

The objective of this work is to contribute toward the development of physics-based engineering wake models by

105 advancing fundamental understandings of the wake dynamics of a utility-scale wind turbine under realistic inflow
 106 with large-scale turbulent flow structures. Turbine-added turbulence increases the dynamic loads on the downwind
 107 turbines. Yang et al. [32] found that the velocity defined by the thrust on the rotor ($U_T = \sqrt{T/\pi R^2}$, where T is the
 108 time-averaged thrust exerted on the turbine rotor, and R the rotor radius) can serve as the proper velocity scale for
 109 the turbine-added turbulence kinetic energy (TKE) of the wake of a turbine located at different downwind locations
 110 from a three-dimensional hill. It was found in [31] that U_T can properly scale the turbine-added TKE for wakes from
 111 turbines of different designs. In the present work, we further examine the velocity U_T for scaling the turbine-added
 112 TKE computed based on wake center locations for a turbine operating with different tip speed ratios under the inflow
 113 with large-scale turbulent flow structures. Meandering describes the low-frequency, large-scale, bodily movement of
 114 turbine wakes. Two mechanisms exist in the literature for the origin of wake meandering. In one mechanism, it
 115 is hypothesized that the meandering is caused by the incoming large-scale turbulent flow structures, which advect
 116 wakes as passive scalars. In the other mechanism, the wake meandering is considered to be the result of the wake
 117 shear layer instability similar to that for the vortex shedding behind bluff bodies. The first mechanism forms the
 118 basis of the dynamic wake meandering model [33]. It was shown in [34] that the predictions from the dynamic wake
 119 meandering model are in good agreement with the field measurements. The second mechanism, on the other hand,
 120 is also supported by wind tunnel experiments [35, 36], numerical simulations [22] and instability analysis [18]. In
 121 particular, meandering frequencies typical for the vortex shedding of bluff bodies were observed in [37] for different
 122 turbine operational regimes and in [31] for different turbine designs ranging from a model wind turbine of diameter 0.13
 123 m to a utility-scale wind turbine of diameter 96 m. In the present work, we numerically examine the effects of the two
 124 mechanisms for a utility-scale turbine under inflows with large-scale turbulent flow structures. To include large-scale
 125 structures in the inflow, we generate the inflow from a precursory simulation using a very large computational domain
 126 and run the simulations sufficiently long to cover the low-frequency motion of the inflow (although it is still not long
 127 enough to ensure an uniformly distributed inflow in the spanwise direction, which will be discussed in section IV),
 128 which is different from our previous work on the simulation of the same turbine [31]. At last we study the probability
 129 density function (PDF) of wake center locations for the simulated cases to examine whether the Gaussian distribution
 130 can model the PDF of wake center locations for the simulated cases.

131 The paper is organized as follows: the following section briefly describes the employed numerical methods including
 132 the flow solver and the actuator surface models for turbine blades and nacelle; the section III describes the compu-
 133 tational setup for both turbine simulations and inflow generation; the section IV presents the computational results;
 134 and the section V draws the conclusions of this paper.

135 II. NUMERICAL METHODS

136 The Virtual Flow Simulator (VFS-Wind) [16, 25, 38, 39] code is employed for simulating the flow past the EOLOS
 137 turbine. VFS-Wind has been systematically validated using wind tunnel and field experiments. Recently, it was
 138 successfully applied to a utility-scale wind farm in complex terrain [40]. The governing equations are the three-
 139 dimensional, unsteady, filtered continuity and Navier-Stokes equations:

$$\frac{\partial u_i}{\partial x_i} = 0, \quad (1)$$

$$\frac{\partial u_i}{\partial t} + \frac{\partial u_i u_j}{\partial x_j} = -\frac{\partial p}{\partial x_i} + \frac{\partial}{\partial x_j} \left(\nu \frac{\partial u_i}{\partial x_j} - \tau_{ij} \right) + f_i, \quad (2)$$

141 where x_i are the Cartesian coordinates, u_i is the i^{th} component of the velocity vector in Cartesian coordinates, ν is
 142 the kinematic viscosity, p is the pressure, f_i are the body forces introduced by the turbine blade and nacelle computed
 143 using the actuator surface models, and τ_{ij} represents the anisotropic part of the subgrid-scale stress tensor, which
 144 is modeled by the dynamic eddy viscosity subgrid-scale stress model [41]. The governing equations are discretized
 145 in space using a second-order accurate central differencing scheme, and integrated in time using the fractional step
 146 method [42]. An algebraic multigrid acceleration along with a GMRES solver is used to solve the pressure Poisson
 147 equation. A matrix-free Newton-Krylov method is used for solving the discretized momentum equations.

148 We briefly describe the actuator surface models for blades and nacelle, respectively. In the actuator surface models,
 149 we have two sets of independent meshes, i.e. the background Cartesian grid for the flow with its coordinate denoted
 150 by \mathbf{x} (x, y, z or x_1, x_2, x_3), and the Lagrangian grid following the actuator surfaces with its coordinate denoted
 151 by \mathbf{X} (X, Y, Z or X_1, X_2, X_3). In the actuator surface model for the rotor blades, the actuator surface is formed
 152 by airfoil chords at different radial locations. In the actuator surface model for nacelle, the actuator surface is the
 153 actual surface of the nacelle. The effects of the blade and nacelle surfaces on the incoming wind are represented by

154 distributed body forces. In general the grid nodes on the actuator surfaces do not coincide with the background fluid
 155 nodes. The smoothed discrete delta function developed in [43] is employed for spreading the forces from the actuator
 156 surfaces to the background grids as follows:

$$f_i(\mathbf{x}) = - \sum_{\mathbf{X} \in g_{\mathbf{x}}} f_i(\mathbf{X}) \delta_h(\mathbf{x} - \mathbf{X}) A(\mathbf{X}), \quad (3)$$

157 where $f_i(\mathbf{X})$ are the forces the air exerts on the turbine structure, and A is the area of the surface mesh element. The
 158 major difference between the actuator surface models for blades and nacelle is how the forces on the actuator surfaces
 159 are computed. In the actuator surface model for blade, the forces are computed using the blade element method as
 160 follows:

$$\mathbf{L} = \frac{1}{2} \rho C_L c |\mathbf{V}_{rel}|^2 \mathbf{e}_L \quad (4)$$

161 and

$$\mathbf{D} = \frac{1}{2} \rho C_D c |\mathbf{V}_{rel}|^2 \mathbf{e}_D, \quad (5)$$

162 where C_L and C_D are the lift and drag coefficients, \mathbf{e}_L and \mathbf{e}_D are the unit vectors for the directions of lift and drag.
 163 To account for the three-dimensional rotational effect and ensure physical behavior of forces near the tip, the stall
 164 delay model developed by Du and Selig [44] and the tip-loss correction proposed by Shen et al. [45, 46] are employed
 165 to correct the lift and drag coefficients, respectively. The relative incoming velocity \mathbf{V}_{rel} employe in Eqs. (4) and (5)
 166 is computed by

$$\mathbf{V}_{rel} = u_x \mathbf{e}_x + (u_\theta - \Omega r) \mathbf{e}_\theta \quad (6)$$

167 at each radial location, where Ω is the rotational speed of the rotor, \mathbf{e}_x and \mathbf{e}_θ are the unit vectors in the axial
 168 and azimuthal directions, respectively. The u_x and u_θ are the axial and azimuthal components of the flow velocity
 169 interpolated from the background grid nodes and averaged over the chord for each radial locations. The computed
 170 lift and drag forces are then uniformly distributed in the chordwise direction at each radial location. In the actuator
 171 surface model for nacelle, the force in the surface normal direction is computed by satisfying the non-penetration
 172 condition as in the direct forcing immersed boundary method, which can be expressed as follows:

$$\mathbf{f}_n(\mathbf{X}) = \frac{h(-\mathbf{u}^d(\mathbf{X}) + \tilde{\mathbf{u}}(\mathbf{X})) \cdot \mathbf{e}_n(\mathbf{X})}{\Delta t} \mathbf{e}_n(\mathbf{X}), \quad (7)$$

173 where $\mathbf{u}^d(\mathbf{X})$ is the desired velocity on the nacelle surface, $\mathbf{e}_n(\mathbf{X})$ is the unit vector in the normal direction of the
 174 nacelle surface, $h = (h_x h_y h_z)^{1/3}$ is the length scale of the local background grid spacing, $\tilde{\mathbf{u}}(\mathbf{X})$ is the estimated velocity
 175 on the actuator surface interpolated from the background grid nodes. The tangential force acting on the surface per
 176 unit area is computed as

$$\mathbf{f}_\tau(\mathbf{X}) = \frac{1}{2} c_f U^2 \mathbf{e}_\tau(\mathbf{X}) \quad (8)$$

177 where c_f is calculated from the empirical relation proposed by F. Schultz-Grunow [47] for turbulent boundary layers
 178 with zero pressure gradient, i.e., $c_f = 0.37(\log Re_x)^{-2.584}$, where Re_x is the Reynolds number based on the incoming
 179 velocity and the distance from the upstream edge of the immersed body, U is the local mean incoming velocity (in
 180 the present cases, it is the mean downwind velocity upwind of the turbine at turbine hub height). For details of the
 181 actuator surface models for blades and nacelle, the reader is referred to [25].

182 III. COMPUTATIONAL SETUP

183 The three-bladed Clipper Liberty 2.5 MW research wind turbine operated by the EOLOS Wind Energy Research
 184 Consortium at the University of Minnesota is employed. Several experimental [26–28] and computational studies [29–
 185 31] have been carried out using this turbine. The power and thrust coefficients of the EOLOS turbine can be changed
 186 by adjusting the blade pitch and the tip-speed ratio (the tip-speed ratio is defined as $\lambda = \frac{\Omega R}{U_h}$, where Ω is the rotor
 187 rotational speed, R is the rotor radius and U_h in the incoming wind speed at hub height). In this work, we focus
 188 on the so-called region 2, in which the blade pitch remains constant and thus we will vary the tip-speed ratio to

189 obtain different thrust coefficients. The diameter of the turbine is $D = 96$ m. The hub height of the turbine is
 190 $z_h = 80$ m. The computational domain size is $L_x \times L_y \times L_z = 22D \times 10D \times 10D$ with the number of grids nodes
 191 $N_x \times N_y \times N_z = 433 \times 339 \times 152$ in the downwind (x), spanwise (y) and vertical (z) directions, respectively. The
 192 wind turbine is located at $x = 0$ and $y = 0$ location. The ground is located at $z = 0$. In the wind turbine and near
 193 wake region, the grid spacings are $\Delta x = \Delta y = \Delta z = D/48$. The height of the computational domain represents the
 194 thickness of atmospheric boundary layer, which is 1 km in the present simulations. Four different tip-speed ratios,
 195 i.e. $\lambda = 6.8, 7.8, 8.8$ and 9.3 , are simulated to represent four different operating conditions. The case with $\lambda = 7.8$
 196 represents the condition close to optimal. It is noted that the different tip-speed ratios are realized in the simulations
 197 by changing the rotor rotational speed instead of the incoming wind speed. Figure 1 shows the power and thrust
 198 coefficients for different tip-speed ratios. It is seen that the C_P increases as the tip-speed ratio increases but starts
 199 decreasing from $\lambda = 7.8$. The C_T increases monotonically as the tip-speed ratio increases from 6.8 to 9.3. In the
 200 next section, we will examine how these changes in the turbine operating condition affect the turbine wake statistics.
 201 Besides the turbine wake simulations, a case without a turbine is also simulated to provide the reference point for

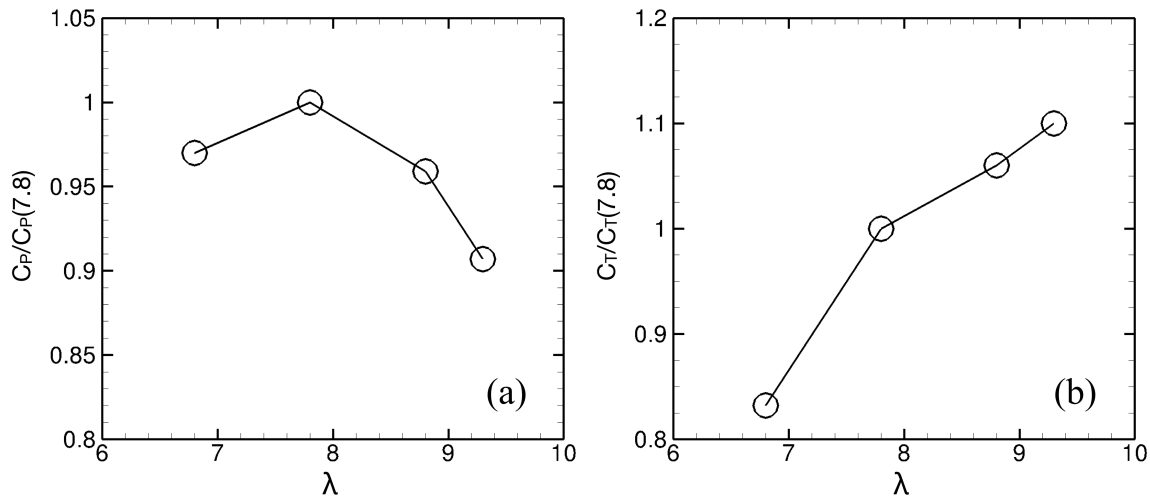


FIG. 1. Power (a) and thrust (b) coefficients for different tip-speed ratios of the EOLOS wind turbine.

202

203

204 analyzing the turbine wake statistics. This no turbine case employs exactly the same grid, time step and inflow
 205 condition as the cases with the turbine. The size of time step is $\Delta t = 0.002D/U_h$ for all the cases. The flowfields are
 206 averaged for about 900 rotor revolutions after the flow is fully developed. This averaging time is significantly longer
 207 than that in [21, 22, 30, 48], and is sufficient to obtain converged statistics of the turbine wakes and capture the
 208 low-frequency motion of the wake. However, it is still not long enough for the incoming flow statistics to be uniformly
 209 distributed in the spanwise direction because of the large temporal scale of the large-scale flow structures captured
 210 by the large computational domain employed in the precursory inflow simulation, which will be described in the next
 211 paragraph. Further averaging can be performed. However the disk storage becomes an issue as each case already
 212 occupied more than 4.7 Terabytes.

213 The incoming turbulent flow at the inlet is generated from a precursory simulation with periodic boundary conditions
 214 in the horizontal directions. Free slip boundary condition is applied at the top boundary. At the wall, the non-
 215 penetration boundary condition is applied to the wall-normal velocity component; for the wall-tangential velocity
 216 component, the shear stress boundary condition is applied with the wall shear stress computed using the
 217 logarithmic law for rough walls, i.e. $\frac{\langle u \rangle}{u^*} = \frac{1}{\kappa} \ln \left(\frac{z}{z_0} \right)$, where $\kappa = 0.4$, $u^* = \sqrt{\tau_w/\rho}$ (τ_w is the wall shear stress), the
 218 roughness length $z_0 = 0.25$ m for the present cases, and $\langle u \rangle$ is given by the first off-wall grid node. The size of the
 219 computational domain for the precursory simulation is 6.2δ , 4.6δ and δ ($\delta = 1$ km is the thickness of the boundary
 220 layer) in the downwind (x), spanwise (y) and vertical (z) directions, respectively. The size of the computational
 221 domain is chosen to be large enough to capture large coherent structures in the atmospheric boundary layer. The
 222 number of grid nodes are $N_x \times N_y \times N_z = 1291 \times 1148 \times 133$. The grid nodes are stretched in the vertical direction
 223 with first off-wall grid spacing $\Delta z = 0.0039\delta$. In the horizontal directions, the grid nodes are uniformly distributed.
 224 The velocity field on a y - z plane is saved at every time step for the inlet boundary condition in the turbine simulations.
 225 The size of the time step employed in the inflow simulation is $0.03D/U_h$. The grid distribution on the y - z plane in
 226 the inflow simulation is different from that in the turbine simulations. Linear interpolation in both time and space is

227 employed to obtain the velocities at the inlet of the turbine simulations. It is also noted that the spanwise dimension
 228 of the inflow simulation domain is significantly larger than that of the turbine simulation. Only a portion of the saved
 229 y-z plane flowfields from the inflow simulation is used in the turbine simulations.

230

IV. RESULTS

231 In this section, we present the computed results from the simulated cases. First we show in figure 2 the inflow
 232 employed in turbine wake simulations. Figure 2(a) and (b) show the time-averaged downwind velocity and TKE
 233 fields on the y-z plane in the precursory simulation employed for inflows for the turbine wake simulations. It is seen
 234 that mild variations in the spanwise direction exist for both the mean downwind velocity and the TKE fields. For
 235 the portion employed for turbine simulations, the incoming wind speed is lower at negative y locations. The TKE
 236 levels are similar at different spanwise locations for $z < 3D$, while are higher in the negative y region for $z > 3D$.
 237 Figure 2(c)–(f) show the mean downwind velocity and TKE profiles at the inlet of the turbine simulation domain. In
 238 figure 2(c), it is seen that the computed vertical profile of the mean downwind velocity agrees well with the logarithmic
 239 law. Figure 2(d) shows that the TKE gradually decreases in the vertical direction from the peak at the near wall
 240 location. This figure also reveals the magnitude and variation of the TKE across the rotor plane in the vertical
 241 direction. Figure 2(e) shows the spanwise variation of the time-averaged downwind velocity at the turbine hub height.
 242 It is seen that the time-averaged downwind velocity slightly varies in the spanwise direction. The velocity at $y > 0$
 243 locations is larger than that at $y < 0$ locations with the downwind velocity at $y = 4R$ being about 6% larger than that
 244 at $y = -4R$. Figure 2(f) shows the spanwise variation of the TKE at turbine hub height. In the remainder of this
 245 section, we will show how such spanwise heterogeneity in the incoming wind and varying turbine operating conditions
 246 affect the wake statistics.

247 Figure 3 depicts the instantaneous downwind velocity fields for cases with different tip-speed ratios. As seen,
 248 the cases with higher tip-speed ratios show, as expected, slightly longer wakes because of higher thrust coefficients.
 249 Despite of the differences in small-scale structures, similarity in large-scale structures is observed between different
 250 cases. We now proceed to examine time and disk-averaged quantities to investigate how wake recovers and how
 251 TKE varies in the downwind direction as a function of tip-speed ratios. The disk used for averaging is of the same
 252 radius as the rotor and is located on the y-z plane at different downwind locations. Figure 4 shows the variation of
 253 time and disk-averaged downwind velocity at different downwind locations. As seen, increasing the tip-speed ratio
 254 from 7.8 decreases the downwind velocity until about $5D$ downwind of the turbine. Decreasing the tip-speed ratio
 255 from 7.8 to 6.8, on the other hand, increases the downwind velocity at almost all considered downwind locations.
 256 Therefore, it is reasonable to speculate that lowering the tip-speed ratio of the upwind turbine may increase the
 257 power of two turbines compared to the situation when the upwind turbine is operating optimally. Figure 5 shows the
 258 downwind variation of (a) the disk-averaged turbulence intensity and (b) the maximum turbulence intensity within
 259 the disk for the three components of velocity fluctuations. As seen, increasing the tip-speed ratio from 7.8 increases
 260 the turbulence intensity at different downwind locations. Decreasing tip-speed ratio from 7.8 to 6.8 decreases the
 261 turbulence intensity except for the disk-averaged downwind component of the turbulence intensity, which increases
 262 in the near wake ($x < 2D$). It is seen that the maximum turbulence intensity in the disk is significantly higher than
 263 the disk-averaged value especially for the downwind component of the turbulence intensity, which is more than 35%
 264 higher.
 265

266 We now examine the velocity deficit and turbine-added TKE profiles computed based on wake center locations. The
 267 velocity deficit and TKE profiles are computed from the time series of spanwise and vertical profiles passing through
 268 $z = z_h$ and $y = 0$, respectively at different turbine downwind locations, which are extracted from the flowfields saved
 269 for every 20 time steps (which means that the time increment is $0.04D/U_h$ between two successively saved flowfields).
 270 The velocity deficit Δu and turbine-added TKE Δk are computed by subtracting those from the simulation without
 271 a turbine as follows:
 272

$$\Delta u = u_{\text{NT}} - u \quad (9)$$

273 for velocity deficits, and

$$\Delta k = k - k_{\text{NT}} \quad (10)$$

274 for TKE, respectively, where the downwind velocity and TKE with a subscript NT and without a subscript are from
 275 the simulations without a turbine and with a turbine, respectively. In order to compute the quantities based on wake
 276 center positions, three regions are identified, i.e. $y_c < -R$, $-R \leq y_c \leq R$ and $y_c > R$ in the spanwise direction,
 277 and $z_c - z_h < -R$, $-R \leq z_c - z_h \leq R$ and $z_c - z_h > R$ in the vertical direction, respectively, where y_c and z_c
 278 are the coordinates of the wake center position in the spanwise and vertical directions, respectively. The wake center
 279

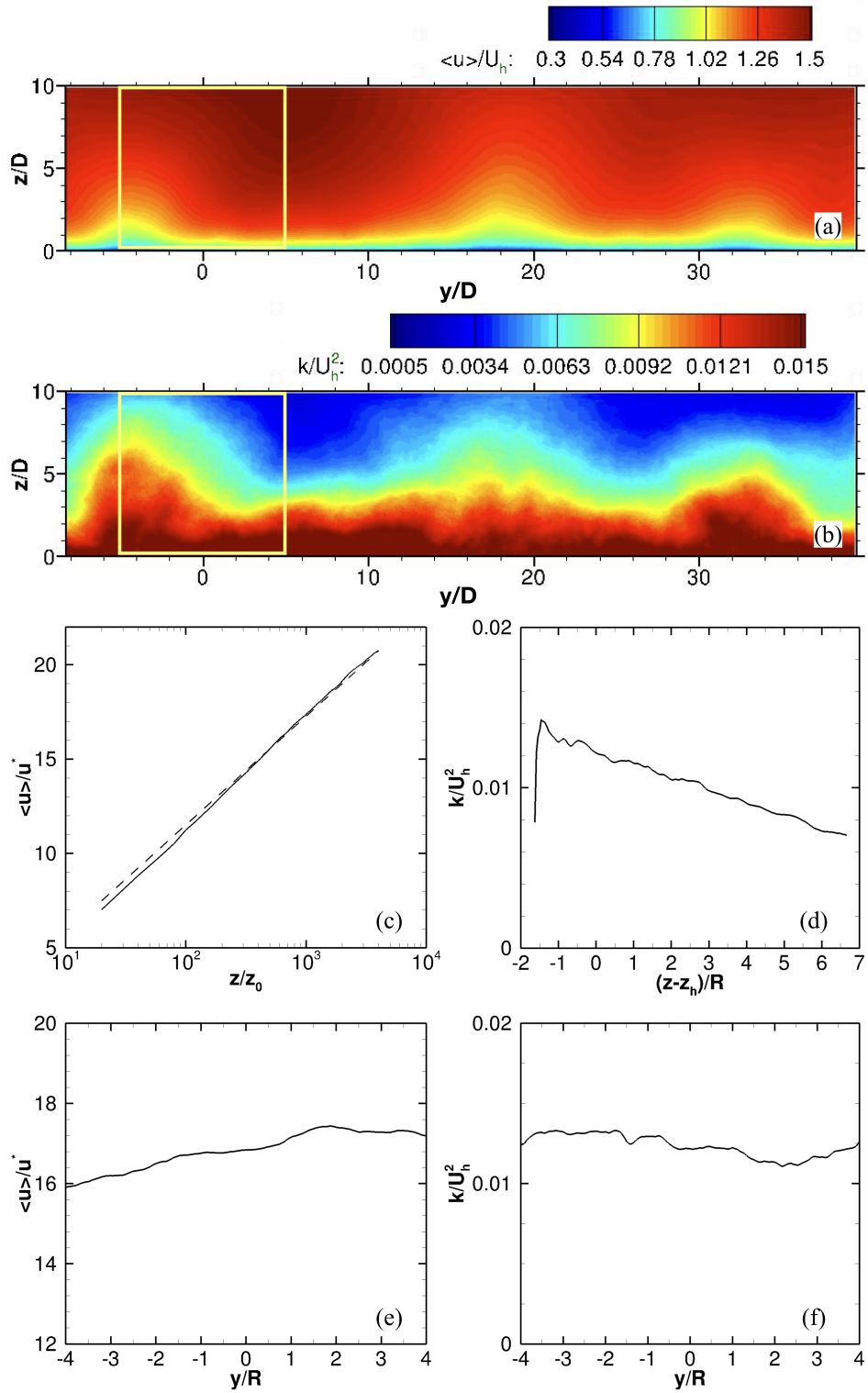


FIG. 2. Statistics of the inflow. (a) and (b) contours of the time-averaged downwind velocity and TKE, respectively on the y - z plane from the inflow simulation, where the instantaneous flowfields are saved for the wind turbine simulation; (c) vertical profiles of the downwind velocity $\langle u \rangle$ (solid line) averaged in time and the spanwise direction and the logarithmic law $\frac{\langle u \rangle}{u^*} = \frac{1}{\kappa} \ln \left(\frac{z}{z_0} \right)$ (dashed line), (d) the vertical profile of the TKE k averaged in time and the spanwise direction, (e) the spanwise profile of the time-averaged downwind velocity at turbine hub height ($z = z_h$) and (f) the spanwise profile of the TKE k at turbine hub height ($z = z_h$). The yellow boxes in (a) and (b) show the part employed in turbine simulations.

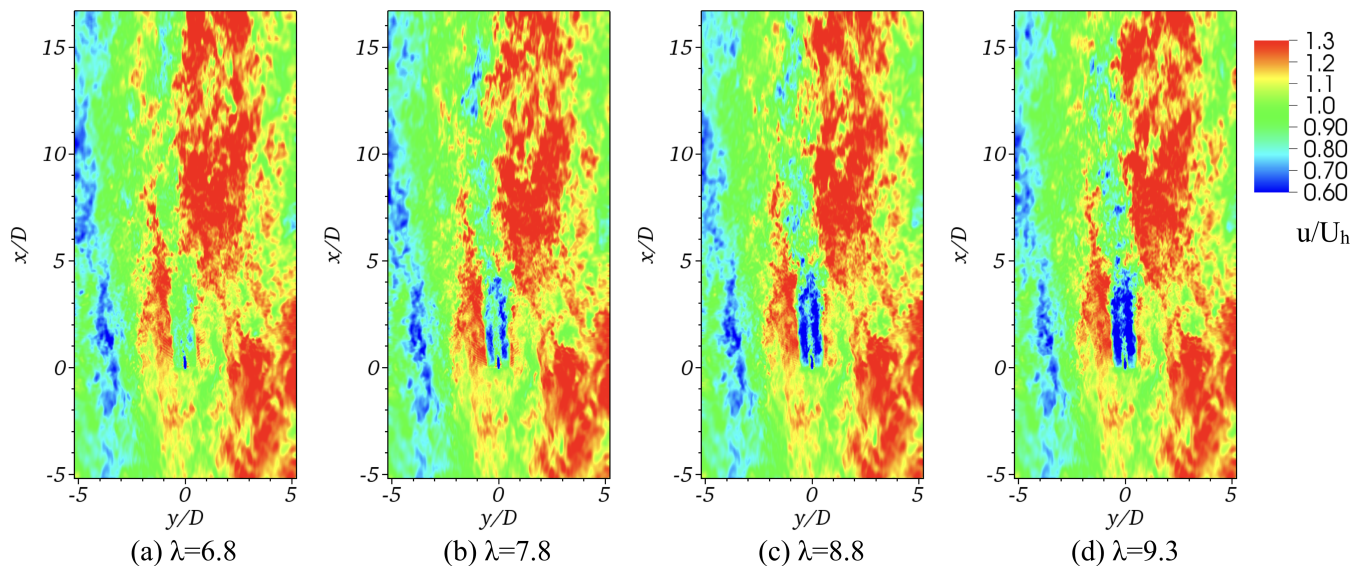


FIG. 3. Contours of the instantaneous downwind velocity on the horizontal plane located at turbine hub height for (a) $\lambda = 6.8$, (b) $\lambda = 7.8$, (c) $\lambda = 8.8$ and (d) $\lambda = 9.3$, respectively.

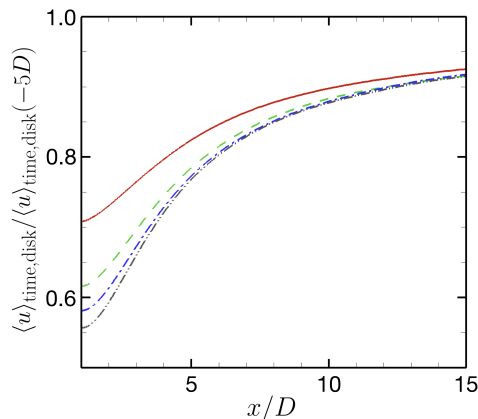


FIG. 4. Variation of time and disk-averaged downwind velocity at different downwind locations. Red solid line: $\lambda = 6.8$; green dashed line: $\lambda = 7.8$; blue dash-dot line: $\lambda = 8.8$; grey dash-dot-dot line: $\lambda = 9.3$.

281 is identified as the location where the maximum Δu occurs using the instantaneous velocity deficit profiles passing
 282 through the rotor centerline. To reduce the effects of the small-scale flow structures on identifying wake centers, the
 283 Δu profiles are filtered using a top-hat filter. Three different filter widths of $0.25D$, $0.5D$ and D are tested to examine
 284 the effects of filter width on identifying wake centers. The identified wake center locations are observed to be similar
 285 for the three filter widths except at the near wake location, i.e. $x = 2D$. In the following results, the filter width $0.5D$
 286 is adopted as in our previous work [21, 31, 49].

287 We show the spanwise and vertical velocity deficit profiles in figures 6 and 7, respectively. It is seen that the
 288 velocity deficit profiles averaged when $-R < y_c < R$ (figure 6(b)) are very similar to those averaged for all wake
 289 center locations (figure 6(a)) and of Gaussian shape at far wake locations. The velocity deficit profiles averaged for
 290 wakes centers in the other two regions (figures 6(c) and (d)), on the other hand, are very different and no longer of
 291 Gaussian shape. It is also observed that the velocity deficits averaged when $y_c < -R$ are larger, which is because of
 292 the lower incoming wind speed in the $y < -R$ region. Although the differences between cases of different tip-speed
 293 ratios are significant at near wake locations, it is noticed that such differences become negligible at far wake locations.
 294 The vertical velocity deficit profiles averaged when $-R < z_c - z_h < R$ (figure 7(b)) are also observed to be very
 295 similar with that averaged for all wake center locations (figure 7(a)). It is also observed that the vertical velocity
 296

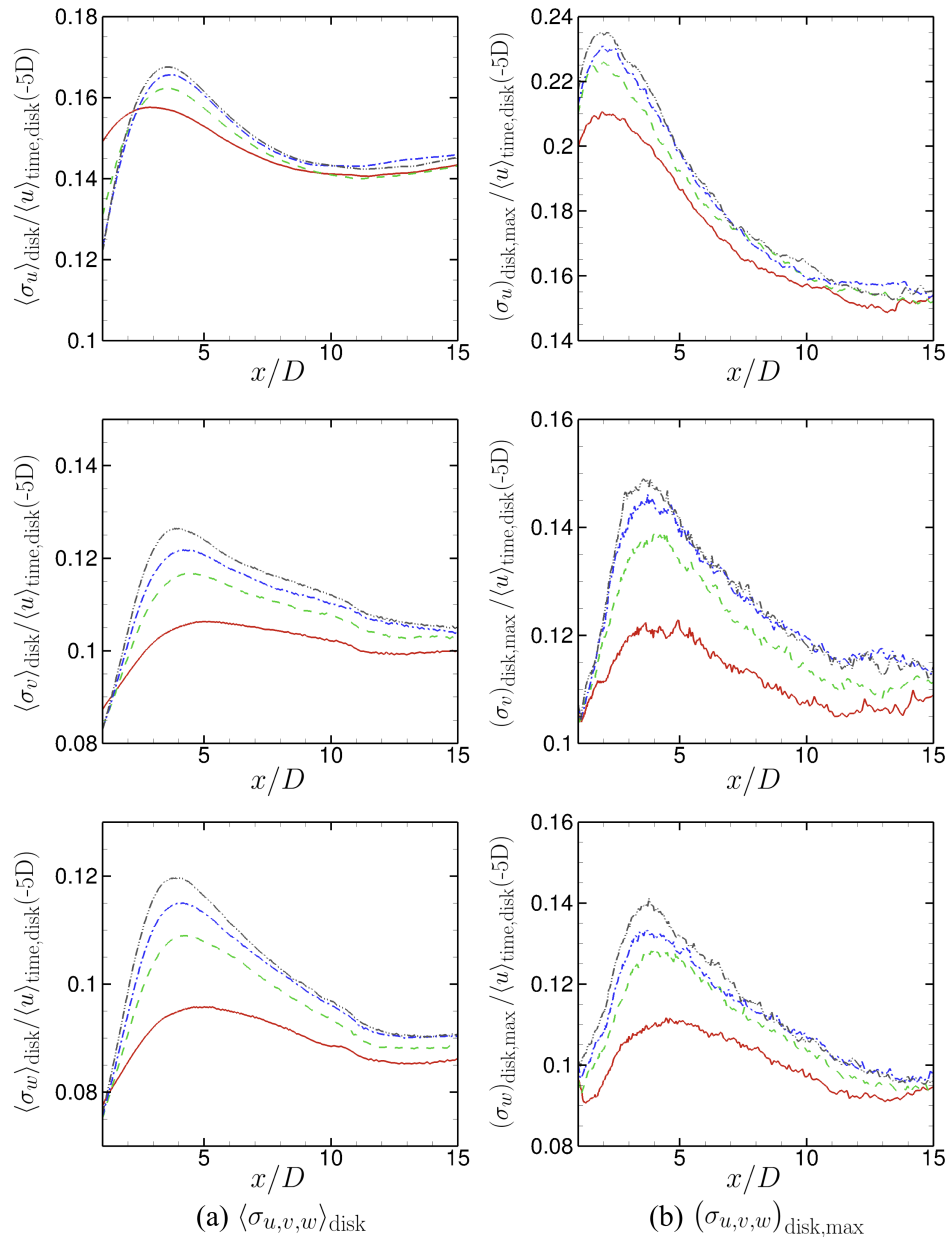


FIG. 5. Downwind variation of (a) the disk-averaged turbulence intensity and (b) the maximum turbulence intensity within the disk for the three components of turbulence intensity, i.e., σ_u , σ_v and σ_w for the downwind, spanwise and vertical components, respectively. Red solid line: $\lambda = 6.8$; green dashed line: $\lambda = 7.8$; blue dash-dot line: $\lambda = 8.8$; grey dash-dot-dot line: $\lambda = 9.3$.

297 deficit profiles for different tip speed ratios are very similar with each other at far wake locations. Because of the wall
 298 blocking effect, the velocity deficit profiles averaged when $z_c - z_h < -R$ (figure 7(c)) are observed to be different from
 299 those averaged for wake centers in the other regions. At $x = 6D, 8D, 10D, 12D$ turbine downwind locations, it is seen
 300 that the vertical velocity deficit profiles averaged when $z_c - z_h < -R$ are composed of two parts, i.e. the nearly linear
 301 part in the $-0.5R < z - z_h < R$ region and the part in the $-1.5R < z - z_h < -0.5R$ region, which is a result of the
 302 interaction of the wake with the wall.

304 We now examine the spanwise and vertical turbine-added TKE profiles in figures 8 and 9, respectively. In our
 305 previous studies, we have shown that normalizing the turbine-added TKE using a velocity scale U_T is able to collapse
 306 the turbine-added TKE profiles for different inflows (caused by different hill-turbine distances) [32] and different
 307 turbine designs [31]. In this work, we examine if such scaling law still works for the turbine-added TKE computed
 308 based on wake center locations and from cases with different tip-speed ratios. Figure 8 shows the spanwise profiles of

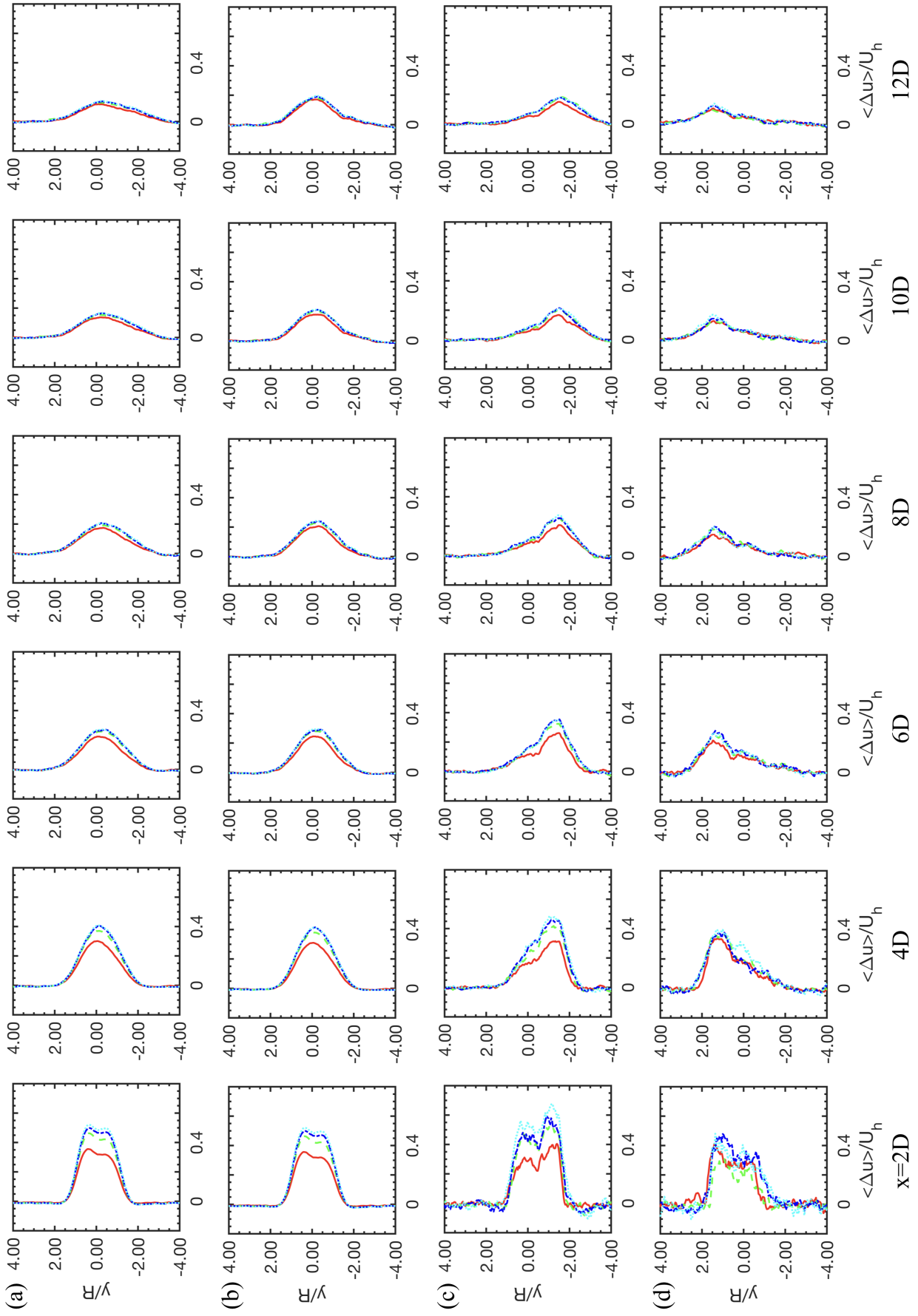


FIG. 6. Spanwise profiles of velocity deficits $\langle \Delta u \rangle$ for (a) averaged for all wake center locations, and (b), (c) and (d) averaged when $-R \leq y_c \leq R$, $y_c < -R$, and $y_c > R$, respectively, at different downwind locations. Red solid line: $\lambda = 6.8$; green dash-dot line: $\lambda = 7.8$; blue dashed line: $\lambda = 8.8$; cyan dotted line: $\lambda = 9.3$.

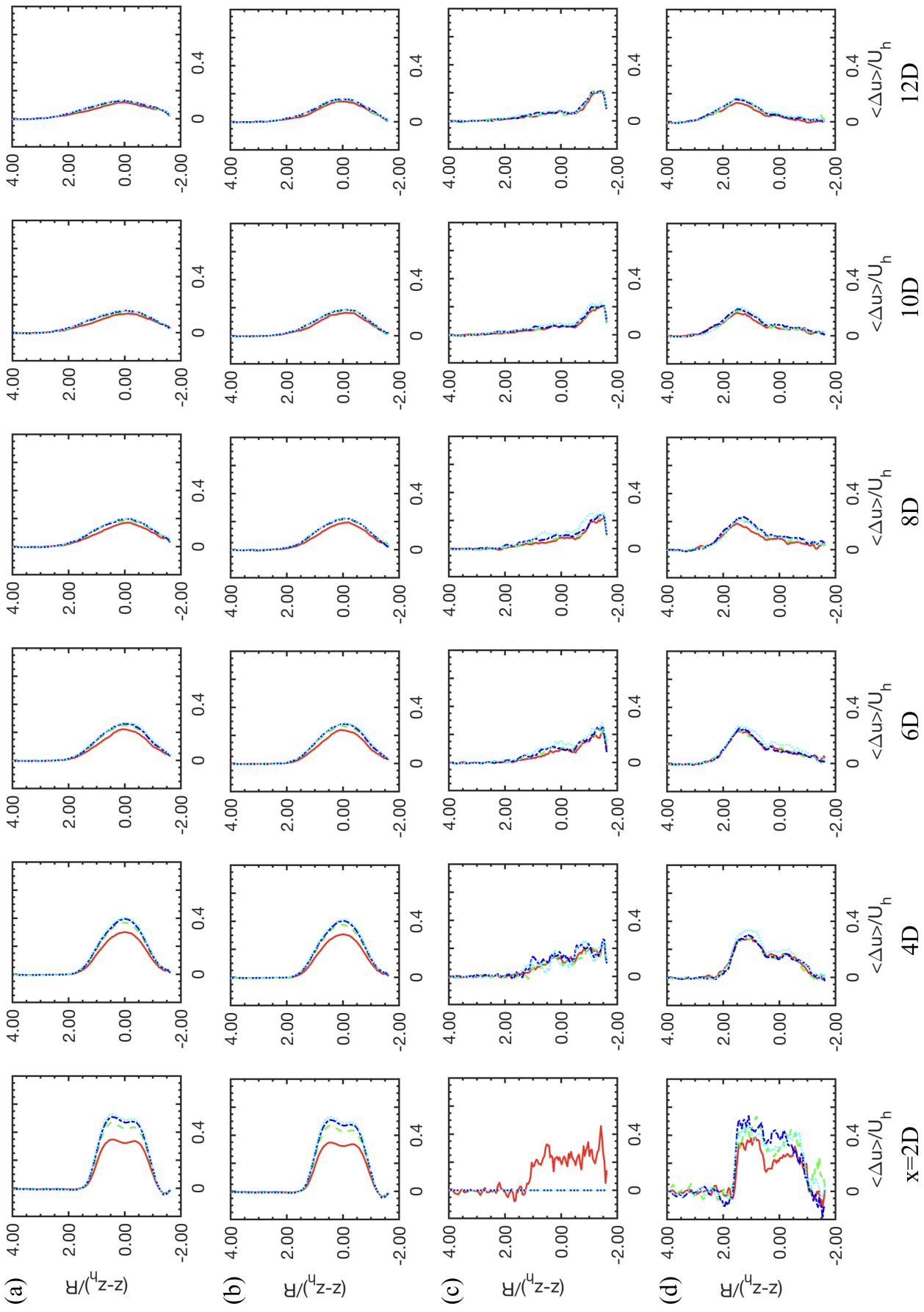


FIG. 7. Vertical profiles of velocity deficits $\langle \Delta u \rangle$ for (a) averaged for all wake center locations, and (b), (c) and (d) averaged when $-R \leq (z_c - z_h) \leq R$, $z_c - z_h < -R$, $z_c - z_h > R$, respectively, at different downwind locations. Red solid line: $\lambda = 6.8$; green dash-dot line: $\lambda = 7.8$; blue dashed line: $\lambda = 8.8$; cyan dotted line: $\lambda = 9.3$.

309 turbine-added TKE. As seen in figure 8(a) for the turbine-added TKE profiles computed for all wake center locations,
 310 two peaks around $y = \pm R$ are observed. It is seen that the peak around $y = R$ is significantly higher than that around
 311 $y = -R$ at $x = 2D, 4D, 6D$ downwind locations. This is because of the higher incoming wind when $y > R$, which
 312 enables faster wake recovery as well as higher TKE. It is also seen that the peak at around $y = -R$ becomes less
 313 significant at $x = 8D$ and negligible at further downwind locations. Figure 8(b) shows the turbine-added TKE profiles
 314 computed when $-R < y_c < R$. As seen, these profiles are very similar to those computed for all wake center locations
 315 as shown in figure 8(a). Figure 8(c) shows the turbine-added TKE profiles computed when $y_c < -R$. As those profiles
 316 in figure 8(a) and (b), two peaks are observed at near wake locations. However, their locations are shifted in the
 317 negative y direction to around $y = 0.5R$ and $y = -2R$ locations, respectively. Figure 8(d) shows the turbine-added
 318 TKE profiles computed when $y_c > R$, where the incoming wind is higher as shown in figure 2. At $x = 4D$ three peaks
 319 at approximately $y = -R, R, 2R$ are observed for the three higher tip-speed ratio cases with the one located around
 320 $y = R$ disappearing at $x = 6D$. One interesting observation from this figure is that the peaks of the turbine-added
 321 TKE persist at much further downwind locations compared with figure 8(a), (b) and (c), which indicates that the
 322 entrainment of high speed wind into the wake is still active at these far wake locations when $y_c > R$. Figure 9 shows
 323 the vertical profiles of the turbine-added TKE. Different from Figure 8, only one peak around $z = z_h + R$ exists in the
 324 vertical direction at the considered downwind locations. As moving in the downwind direction, the profiles are very
 325 similar to each other although the magnitude of TKE decreases. The turbine-added TKE profiles computed when
 326 $-R < z_c - z_h < R$ are shown in figure 9(b). It is seen that the turbine-added TKE profiles in figure 9(b) are very
 327 similar to that in 9(a), although the magnitudes of TKE are somewhat lower in figure 9(b) at far wake locations.
 328 The turbine-added TKE profiles computed when $z_c - z_h < -R$ are shown in figure 9(c). One interesting observation
 329 (which is also observed in figures 8 and figures 9(a), (b) and (d) but not as clearly as in figure 9(c)) is that the
 330 Δk values are negative in the $z - z_h < -R$ region, which indicates that the turbine wake suppresses the turbulent
 331 fluctuations near the wall. The turbine-added TKE profiles computed when $z_c - z_h > R$ are shown in figure 9(d).
 332 One major difference compared with figures 9(a), (b) and (c) is that there are two peaks located around $z - z_h = 0$
 333 and $z - z_h = 2R$ locations, respectively, which indicates that significant amount of momentum is entrained into the
 334 wake from both the upper and lower boundaries of the wake when $z_c - z_h > R$. Finally, we want to emphasize the
 335 most important observation from figures 8 and 9 is that the turbine-added TKE profiles computed based on wake
 336 center locations collapse well with each other at $x = 6D$ and further downwind locations when normalized by U_T .
 337
 338

339 We have seen the similarity of large-scale flow structures from the instantaneous flowfields as shown in figure 3.
 340 To further examine such similarity in turbine wakes, we show the power spectral density (PSD) of the spanwise
 341 velocity fluctuations along the rotor centerline at different downwind locations in figure 10. The PSD is computed
 342 using Welch's method [50]. The velocity at every time step (the size of time step is $\Delta t = 0.002D/U_h$) is recorded for
 343 computing the PSD. The total number of time steps is 200000. For the PSD profiles presented in this section, we
 344 employ $L = 100000$ (the length of each segment), $S = 20000$ (the separation between two adjacent segments) and the
 345 W_2 window function, which will be defined in the appendix, for computing the PSD using Welch's method. Figure 10
 346 shows the PSD at $2D$ turbine upwind. As seen, a significant amount of energy exists at a very low frequency of
 347 $fD/U_h \approx 0.01$ in the inflow. It is interesting to see that this low frequency motion from the inflow persists at $5D$,
 348 $10D$ and $15D$ turbine downwind locations as shown in figures 10(b), (c) and (d), respectively. The PSD levels of
 349 the low frequency motion with $fD/U_h \approx 0.01$ are either increased or decreased at these turbine downwind locations
 350 in comparison with that at $x = -2D$. The downwind variations of the PSD levels for different frequencies will be
 351 examined in figure 11. It should be noticed that the blade passing frequency (which is $fD/U_h \approx 6.3 \sim 8.6$ for the
 352 present cases) is not discernible in figures 10(b), (c) and (d) for two reasons: 1) the spanwise velocity fluctuations
 353 are recorded at turbine hub height where the wake is dominated by the nacelle wake; and 2) the signature from the
 354 rotor's rotational motion is significantly attenuated at $5D$, $10D$ and $15D$ turbine downwind locations. Besides the
 355 low frequency motion from the incoming flow, the wake is also dominated by another relatively higher frequency
 356 of $fD/U_h \approx 0.15$ as shown in figures 10 (b), (c) and (d), which is the frequency of the large-scale motion of the
 357 wake caused by the wake shear layer instability similar to that of the vortex shedding behind bluff bodies. Both
 358 frequencies describe the large-scale motion of the turbine wake. In this paper, we refer the wake motion of frequency
 359 $fD/U_h \approx 0.15$ as the shear-induced meandering motion, and the wake motion of frequency $fD/U_h \approx 0.01$ as the
 360 inflow-driven meandering motion, respectively, for differentiating the large-scale motion of the wake at two different
 361 frequencies. Now we examine how the turbine and the wake interact with the incoming turbulence at different scales,
 362 i.e. from the large-scale motion at frequency of $fD/U_h \approx 0.01$ to the shear-induced wake meandering motion at
 363 frequency of $fD/U_h \approx 0.1 \sim 0.2$ and wake motion at frequencies higher than the frequency of the shear-induced wake
 364 meandering motion. To do this, we divide the frequencies into four regions, i.e. $fD/U_h \leq 0.02$, $0.02 < fD/U_h \leq 0.14$,
 365 $0.14 < fD/U_h \leq 0.2$ and $0.2 < fD/U_h \leq 0.32$, which we denote as low, intermediate, shear-induced meandering and
 366 high frequencies, respectively. In each region, the maximum PSD at each downwind location is found and plotted in
 367 the right column of figure 11 with the corresponding frequency plotted in the left column of figure 11, respectively.
 368 First we examine the downwind variation of the frequencies with the maximum PSD level in the left column of
 369

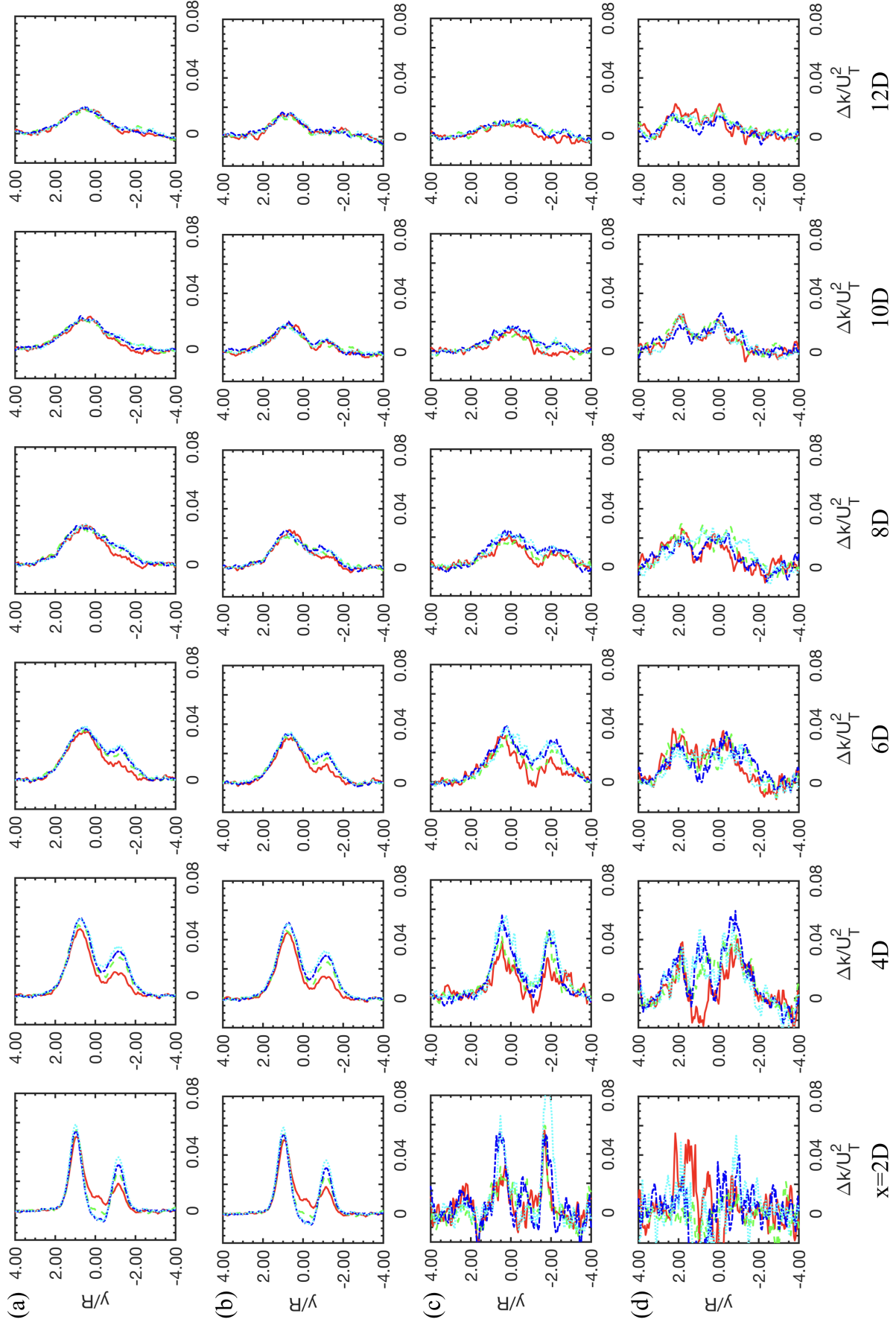


FIG. 8. Spanwise profiles of turbine-added TKE, Δk for (a) computed for all wake center locations, and (b), (c) and (d) computed when $-R \leq y_c \leq R$, $y_c < -R$, and $y_c > R$, respectively, at different downwind locations. Red solid line: $\lambda = 6.8$; green dash-dot line: $\lambda = 7.8$; blue dashed line: $\lambda = 8.8$; cyan dotted line: $\lambda = 9.3$.

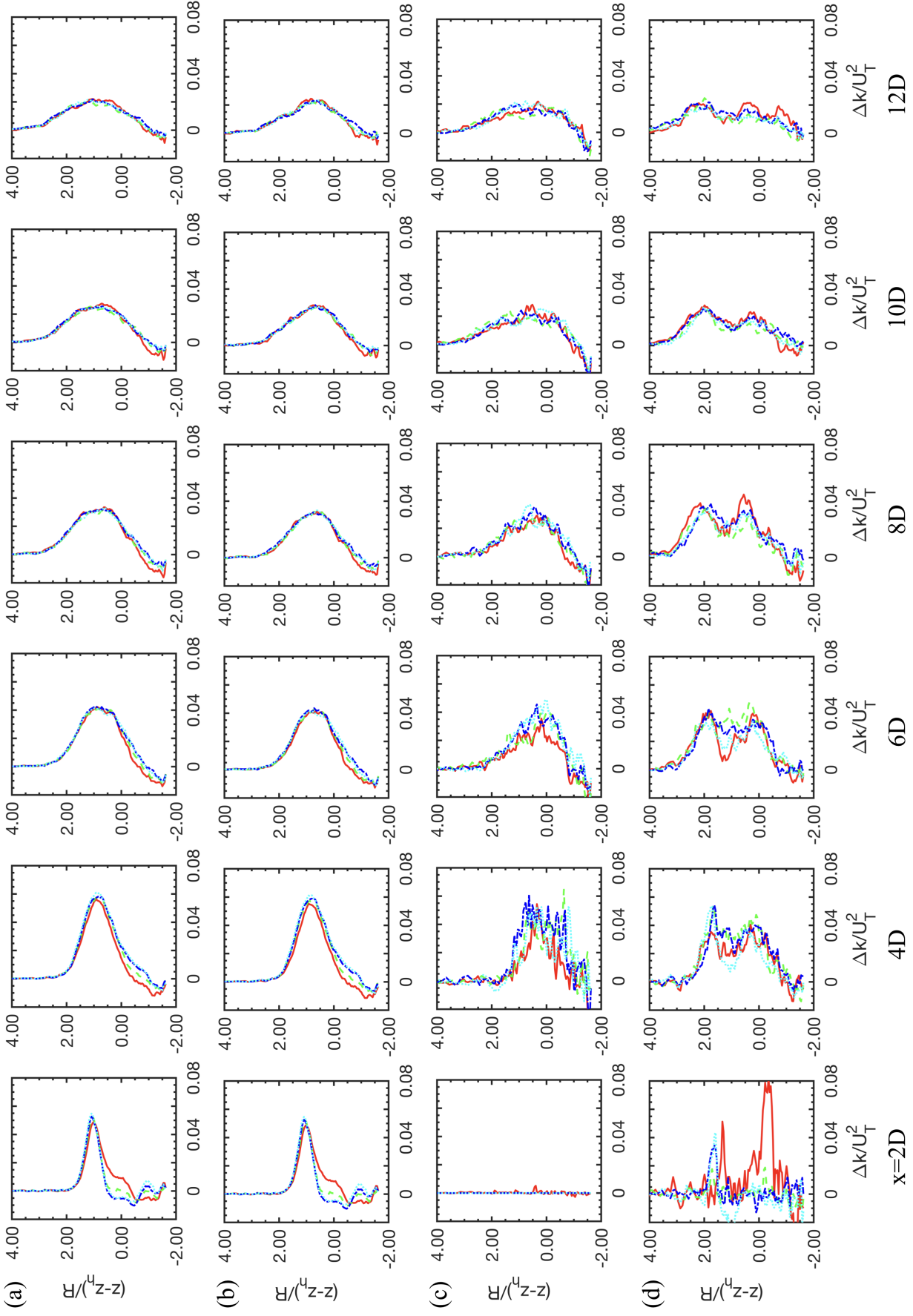


FIG. 9. Vertical profiles of turbine-added TKE Δk for (a) computed for all wake center locations, and (b), (c) and (d) computed when $-R \leq (z_c - z_h) \leq R$, $z_c - z_h < -R$, $z_c - z_h > R$, respectively, at different downwind locations. Red solid line: $\lambda = 7.8$; green dash-dot line: $\lambda = 8.8$; cyan dotted line: $\lambda = 9.3$.

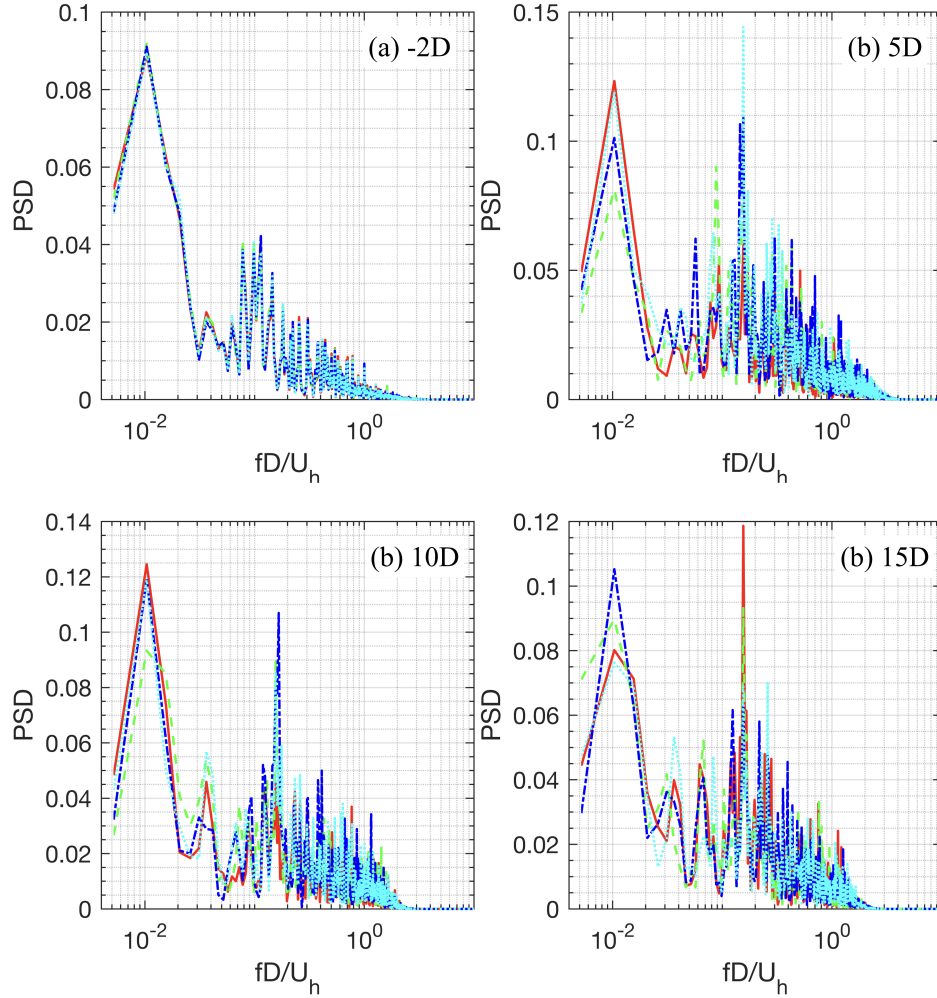


FIG. 10. PSD profiles from cases of different tip-speed ratios at different downwind locations. The PSD is computed using the spanwise velocity fluctuations at different turbine downwind locations along the rotor centerline and normalized by the variance at $x = -2D$. Red solid line: $\lambda = 6.8$; Green dashed line: $\lambda = 7.8$; Blue dash-dot line: $\lambda = 8.8$; Cyan dotted line: $\lambda = 9.3$.

370 figure 11. We can see on the left of figure 11(a) that the dominant frequency in the low frequency region (frequency
 371 of the inflow-driven meandering at far wake locations) persists at $fD/U_h \approx 0.01$ for most downwind locations until
 372 $x = 10D$, and shifts to a higher value at further downwind locations for some cases. The shear-induced meandering
 373 frequency as shown on the left of figure 11(c) stays at around $fD/U_h \approx 0.15$ starting from $x = 3D \sim 4D$ for all the
 374 cases. The dominant frequencies in the other two regions, on the other hand, fluctuate vibrantly for all the cases
 375 as shown on the left in figure 11(b) and (d). Now we examine the downwind variation of the maximum PSD level
 376 in the right column of figure 11. The PSD level of the low frequency motion (inflow-driven meandering at far wake
 377 locations) at $fD/U_h \approx 0.01$ decreases until $x \approx 2D$ to about 50% of that at $x = -2D$. The PSD levels in the regions
 378 of intermediate frequency, shear-induced meandering frequency and high frequency, on the other hand, increase as
 379 approaching the turbine and decrease to the minimum at $x \approx 2D$. From $x \approx 2D$ the maximum PSD levels in the
 380 four frequency regions start increasing to a plateau at around $x \approx 4D \sim 5D$. The PSD levels at $x > 4D$ locations
 381 are similar for different cases, except that the PSD levels of the $\lambda = 6.8$ case are smaller than the other cases in the
 382 intermediate and shear-induced meandering frequency regions for $5D < x < 12D$.

384 So far we have examined the disk-averaged statistics, statistics based on wake center locations and the PSD of
 385 velocity fluctuations for different operating conditions. Now we investigate the statistics of wake center locations,
 386 which are useful for developing the wake steering technique to alleviate the negative impacts of wakes on downwind
 387 turbines. As mentioned the velocity deficits defined as $\Delta u = u_{NT} - u$ (with the mean plotted in figure 6(a) and
 388 figure 7(a)) are used to detect wake center locations. Figure 12 shows the wake center locations at different downwind
 389 locations for the entire simulation time for tip speed ratio $\lambda = 7.8$. In this figure, the wake center is identified as

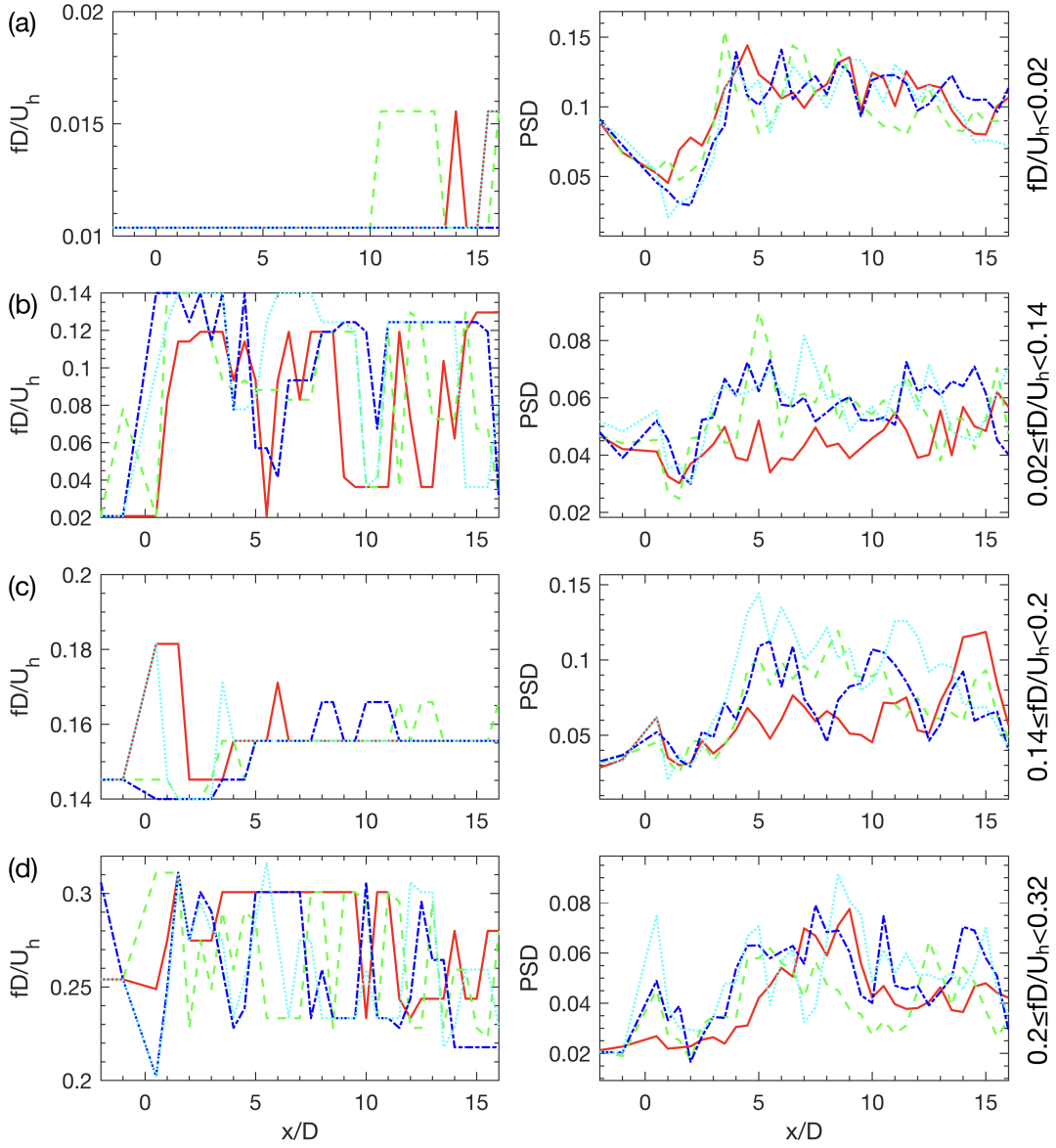


FIG. 11. Downwind variations of the maximum PSD and the corresponding frequency in the four regions of different ranges of frequency for (a) $0.01 \leq fD/U_h < 0.02$, (b) $0.02 \leq fD/U_h < 0.14$, (c) $0.14 \leq fD/U_h < 0.2$ and (d) $0.2 \leq fD/U_h < 0.32$, respectively. The PSD is computed using the spanwise velocity fluctuations at different downwind locations along the rotor centerline and normalized by the variance at $x = -2D$. Red solid line: $\lambda = 6.8$; Green dashed line: $\lambda = 7.8$; Blue dash-dot line: $\lambda = 8.8$; Cyan dotted line: $\lambda = 9.3$. It is noticed that the data are sampled every $0.5D$ and $1D$ in the turbine downwind and turbine upwind direction, respectively.

390 the location of the maximum of the instantaneous velocity deficits Δu on y - z planes at different downwind locations.
 391 To reduce the uncertainties, a spatial filtering on the y - z plane with the filter width of $0.5D$ is performed on the
 392 instantaneous velocity deficit field similar to the work in [19, 21]. As seen at the near wake locations ($x < 3D$), the
 393 wake center positions are confined within a small circle of radius less than the rotor radius. The region having wake
 394 centers gradually increases in both spanwise and vertical directions in the downwind direction. Starting from $x \approx 4D$,
 395 the radius of the wake center region is larger than the rotor radius while from around $x = 6D \sim 7D$ wake centers are
 396 detected in the near wall region as a result of wake expansion and its interaction with the wall. Starting from around
 397 $x = 6D \sim 7D$, the radius of the wake center area in the spanwise direction is observed to be larger than the rotor
 398 diameter. At very far downwind locations (e.g. $x > 13D$), the wake center area ranges approximately $-2D < y < 2D$
 399 and $0 < z < 1.5D$ in the spanwise and vertical directions, respectively. Our simulations reveal similar wake center

400 scattering as in figure 12 for the other different tip-speed ratios.

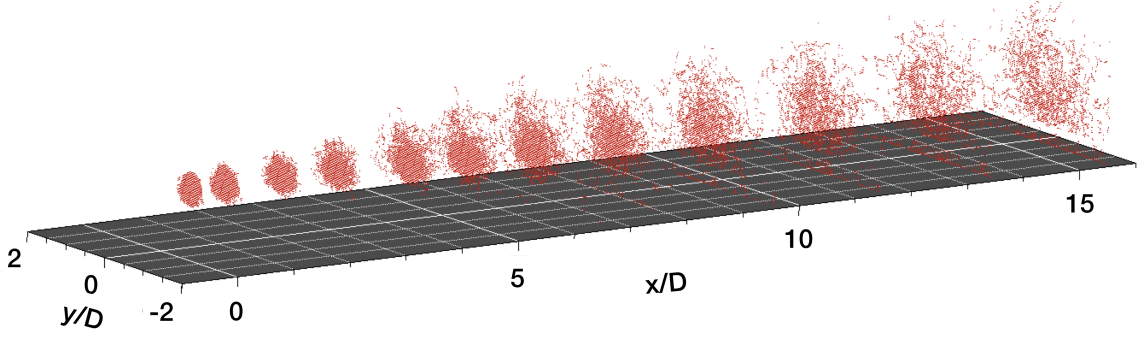


FIG. 12. Scattered points showing instantaneous wake center locations at different downwind locations for the entire simulation time. Tip-speed ratio $\lambda = 7.8$.

401

402

403

404

405

406

407

408

409

410

411

412

413

Subsequently we compare the PDF profiles of wake center locations in the spanwise and vertical directions. Figure 13 shows the PDF of wake center locations in the spanwise direction at different downwind locations. The thick black line in each subplot shows the fitted Gaussian distribution. At $2D$ turbine downwind, some deviations from the Gaussian distribution are observed near the peak of the PDF. At $4D$ and $6D$ downwind locations, an overall good agreement of the computed PDF with the Gaussian distribution is observed although some minor differences are still observed. At $x = 8D$ and further downwind locations, the differences between the computed PDF and the fitted Gaussian distribution are significant. As seen, the computed PDF indicates a higher probability for the wake centers in the region around the mean wake center while a lower probability in the region away from the mean wake center compared with the fitted Gaussian distribution. Similar field observation but at $4D$ turbine downwind was reported in [51]. At $x = 12D$, the computed PDF is also significantly skewed that the wake centers have a lower probability in the positive y side than in the negative y side. Figure 14 shows the PDF of wake center locations in the vertical

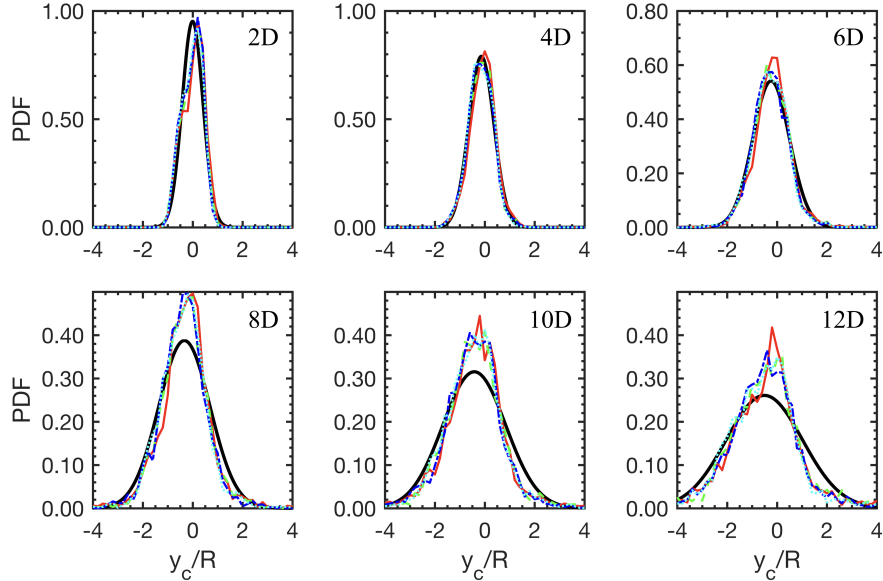


FIG. 13. PDF of wake center locations in the spanwise direction at turbine hub height and different turbine downwind locations. Red solid lines: $\lambda = 6.8$; green dashed lines: $\lambda = 7.8$; blue dash-dot lines: $\lambda = 8.8$; cyan dotted lines: $\lambda = 9.3$. The thick black lines represent the fitted Gaussian distribution with the mean and standard deviation averaged from four cases.

414

415

416

417

418

direction at different downwind locations. The same as in figure 13, the computed PDF slightly deviates from the Gaussian distribution around the peak of the PDF at $2D$ turbine downwind location especially for the $\lambda = 6.8$ case. At $x = 4D$ turbine downwind location the Gaussian distribution reasonably approximates the computed PDF although

419 some minor differences are still observed. The probability for wake centers in the region close to ground is observed
 420 to be high at $x = 6D$ turbine downwind location and gradually increases at further turbine downwind locations. The
 421 PDF in the near ground region cannot be modeled by the Gaussian distribution, though the Gaussian distribution
 422 seems to be an acceptable approximation in the region away from the ground. From figures 13 and 14, we can see
 423 that the Gaussian distribution is an acceptable approximation to the computed PDF distributions at $x = 2D, 4D, 6D$.
 424 At $x = 8D$ and further downwind locations, significant differences between the Gaussian distribution and computed
 425 PDF distributions are observed. In spite of the different fitness of the computed PDF to the Gaussian distribution
 426 at different downwind locations, the computed PDF from different cases collapse well with each other at almost all
 427 considered downwind locations.

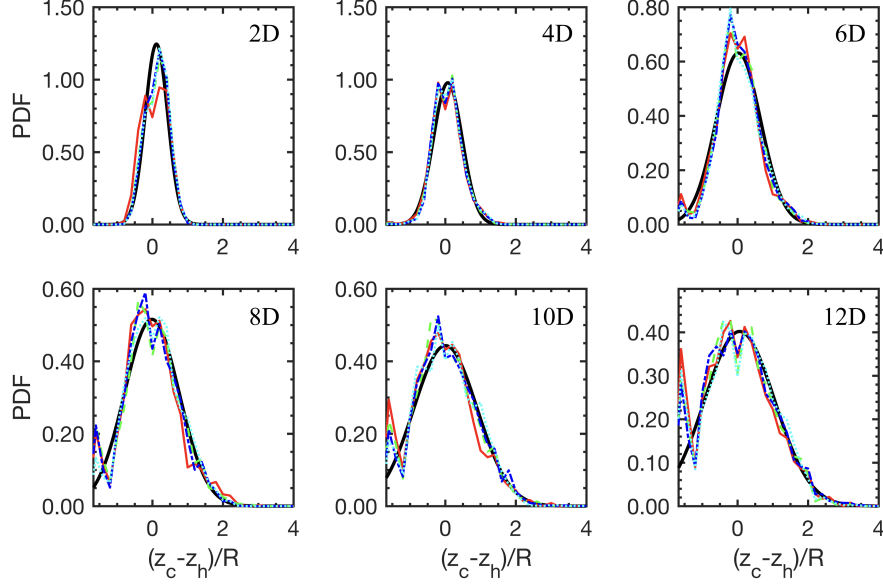


FIG. 14. PDF of wake center locations in the vertical direction along the rotor centerline at different turbine downwind locations. Red solid lines: $\lambda = 6.8$; green dashed lines: $\lambda = 7.8$; blue dash-dot lines: $\lambda = 8.8$; cyan dotted lines: $\lambda = 9.3$. The thick black lines represent the fitted Gaussian distribution with the mean and standard deviation averaged from four cases.

428

429

430 To further quantify how well the PDF of wake center locations can be represented by the Gaussian distribution,
 431 we plot in figure 15 the skewness and kurtosis of wake center locations. First we examine the skewness and kurtosis
 432 of wake center fluctuations in the spanwise direction as shown in figure 15(a) and (c), respectively. As seen the
 433 values of skewness and kurtosis from different cases are similar to each other and close to 0 and 3, respectively for
 434 $x < 5D$ indicating that in this region the PDF of wake center locations can be reasonably represented by the Gaussian
 435 distribution. For $x > 5D$, however, the skewness and kurtosis from different cases are much scattered and significantly
 436 deviate from 0 and 3, respectively, which means that the Gaussian distribution is not a proper choice in this region.
 437 In figure 15(b) and (d) we examine the skewness and kurtosis of wake center fluctuations in the vertical direction.
 438 Similar trends with that in the spanwise direction are observed. However, the skewness and kurtosis become scattered
 439 at about $x = 9D$ much later than the spanwise direction.

441 After examining the PDF of the wake center locations, we show the downwind variations of the mean wake center
 442 locations and the standard deviation of wake center fluctuations in figure 16. First we examine the mean of wake
 443 center locations in figure 16(a) and (b). As seen the mean wake center moves to the negative y direction as the wake
 444 travels in the downwind direction. This is because of the spanwise heterogeneous distribution of the incoming wind
 445 which is higher at the positive y side compared with that at the negative y side. It is interesting to see that the
 446 slope is nearly constant, although it is somewhat higher from $2D$ to $4D$ turbine downwind. Figure 16(b) shows the
 447 downwind variation of the wake centers in the vertical direction. As seen two stages exist for the downwind variations
 448 of wake centers z_c . From $1D$ turbine downwind to $9D$ turbine downwind the wake centers move toward the wall,
 449 while from $9D$ to $16D$, the wake centers move away from the wall. It is noticed that at $x = 9D$, where the wakes
 450 bounce away from the ground, is exactly the same location where the skewness and kurtosis of the vertical wake
 451 center locations become scattered as shown in figure 15(b) and (d). This observation is similar for cases of different
 452 tip-speed ratios except for the case of tip-speed ratio $\lambda = 6.8$, for which the minimum wake center in the vertical
 453 direction is much lower than the other cases and happens at much further turbine downwind location (about $10D$ to

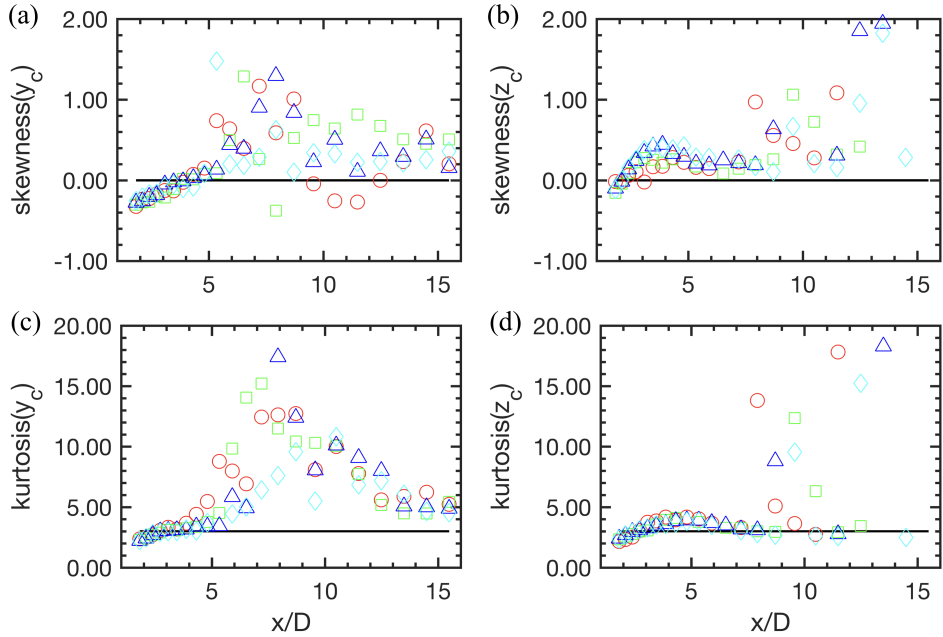


FIG. 15. Skewness and kurtosis of wake center locations for (a) and (c) in the spanwise direction and (b) and (d) in the vertical direction, respectively at different downwind locations. Red circles: $\lambda = 6.8$; green squares: $\lambda = 7.8$; blue triangles: $\lambda = 8.8$; cyan diamonds: $\lambda = 9.3$.

454 11D). It is also noticed that the magnitudes of the slopes are nearly the same for the two stages. In figure 16(c), we
 455 show the downwind variations of the standard deviations of the wake center fluctuations in the spanwise direction.
 456 Two stages similar with that in figure 16(a) are observed. In the first stage σ_{y_c} remains nearly the same from $2D$ to
 457 about $4D$ turbine downwind, where the wake meandering has not yet started and wake centers fluctuate in a very
 458 confined region. In the second stage from $x = 4D$, a linear increase is observed. Figure 16(d) shows the downwind
 459 variations of the standard deviations of wake center fluctuations in the vertical direction. Different from figures 16(a)
 460 and (c), three stages are observed. The first stage is very similar to that in figure 16(a), where σ_{z_c} remains nearly
 461 constant from $2D$ to $4D$ turbine downwind. In the second stage from $4D$ to about $7D$ turbine downwind, σ_{z_c} grows
 462 linearly at a rate similar to that in the second stage of figure 16(c). In the third stage, on the other hand, σ_{z_c}
 463 grows linearly at a rate about half of the rate of the second stage from $7D$ until $16D$ turbine downwind. For the
 464 downwind variations of both the mean center locations and the standard deviations of the wake center fluctuations,
 465 one important observation is that the profiles collapse well with each other for the four different cases with different
 466 operating conditions. Such similarity implies scaling laws for describing the downwind variations of the mean wake
 467 center locations and the standard deviation of the wake center fluctuations. Development of such scaling laws will
 468 be carried out based on wake data from different turbines, operating conditions and inflow conditions in our future
 469 work.
 470

471 V. CONCLUSIONS

472 We investigated the wake of the EOLOS 2.5 MW Clipper turbine under different operating conditions using LES
 473 with the actuator surface models for turbine blades and the nacelle. Four cases with different tip-speed ratios
 474 and one case without a turbine under exactly the same inflow were carried out. The inflow was generated from a
 475 precursory simulation using a very large computational domain to include the large-scale flow structures existing in the
 476 atmospheric turbulence. The velocity deficits and the turbine-added TKE computed based on different wake center
 477 locations were analyzed. We found that the velocity deficit profiles and the turbine-added TKE profiles computed
 478 for wake centers directly in the downwind of the turbine are nearly the same as those computed for all wake center
 479 locations, while those computed when wake centers are above the top tip, below the bottom tip, or off the tips in the
 480 spanwise direction are significantly different. At far wake locations (starting from about $6D$ turbine downwind) we
 481 found that the incoming wind speed at the turbine hub height and the velocity defined by the thrust on the rotor are
 482 the proper velocity scales for the velocity deficits and turbine-added TKE computed based on different wake center

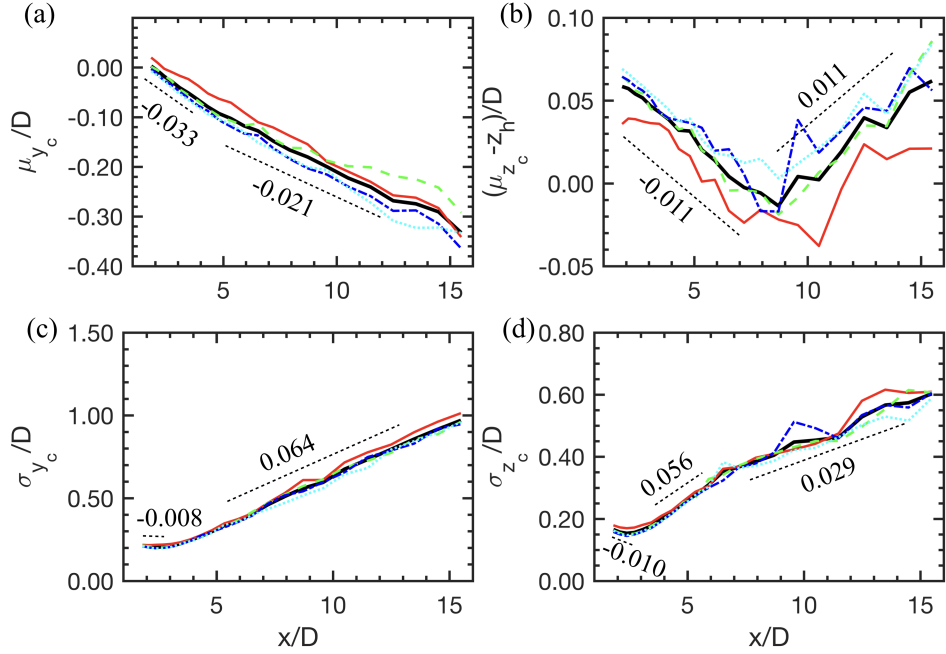


FIG. 16. Mean and standard deviation of wake center locations for (a) and (c) in the spanwise direction and (b) and (d) in the vertical direction, respectively at different downwind locations. Red solid lines: $\lambda = 6.8$; green dashed lines: $\lambda = 7.8$; blue dash-dot lines: $\lambda = 8.8$; cyan dotted lines: $\lambda = 9.3$. The thick black lines represent the Gaussian fitted mean and standard deviation averaged over the four cases. The black dashed lines show the best-fitted slopes of the thick black lines.

483 locations for all tip-speed ratio cases. We investigated the power spectral density (PSD) from different cases and
 484 found that the frequency of the large-scale flow structures from the inflow persists in the turbine wake at different
 485 turbine wake locations for all cases, which indicates the large-scale motion of turbine wakes caused by the inflow large-
 486 scale eddies, the so-called inflow-driven wake meandering in the present paper. The other dominant frequency of the
 487 large-scale motion of turbine wakes is also observed at turbine far wake locations starting at about $3D \sim 4D$ turbine
 488 downwind for all the cases. The second dominant frequency is of Strouhal number 0.15 typical for the frequency of
 489 vortex shedding behind bluff bodies, which indicates the wake shear layer instability also causes the large-scale motion
 490 of turbine wakes, the so-called shear-induced wake meandering in the present paper. We further divide a range of
 491 frequency into four regions, i.e. the low frequency region where the frequency of the inflow large-scale flow structures
 492 is located, the intermediate frequency region of frequencies higher than the incoming low frequency but lower than
 493 the frequency of the shear-induced wake meandering, the frequency region of the shear-induced wake meandering,
 494 and the high frequency region with frequencies higher than the frequency of shear-induced meandering. It is observed
 495 that the PSD level of the inflow low frequency motion decreases as approaching the turbine and in the turbine's near
 496 wake, which was recently observed in the measurements and termed the sheltering effect of the turbine [52]. At far
 497 wake locations ($x > 4D \sim 5D$) the maximum PSD levels in the four regions are increased for all the cases except
 498 for the $\lambda = 6.8$ case, in which the increases are not significant in the intermediate and the shear-induced meandering
 499 frequency regions. We also investigated the profiles of probability density function (PDF) of the wake center locations
 500 at different downwind locations. We found that the PDF profiles from all the cases of different tip-speed ratios collapse
 501 with each other for almost all the downwind locations. At $2D$, $4D$ and $6D$ turbine downwind locations, the PDF
 502 profiles can be reasonably approximated by the Gaussian distribution. At further turbine downwind locations, on
 503 the other hand, the PDF profiles deviate from the Gaussian distribution. To further test the validity of the Gaussian
 504 distribution for the PDF of wake center locations, the skewness and kurtosis of the wake center fluctuations were
 505 examined. Finally, we examined the downwind variations of the mean values and the standard deviations of wake
 506 center fluctuations and found that they collapse with each other for all the considered tip-speed ratios.

507 In this study, the employed incoming wind is somewhat lower in the $y/R < 0$ region (the turbine is located at
 508 $y/R = 0$). This causes a higher probability for wake centers in the $y/R < 0$ region, which then affects the wake
 509 statistics that depend on the spanwise locations (figures 6, 8 and 13). However, this does not affect the similarity
 510 we observed from different tip-speed ratio cases as the inflow applied is exactly the same. The computed results also
 511 indicate the possibility to model the inflow effect on the spanwise wake center displacement as shown in figure 16,

which is useful for computing wake statistics for a period of time not long enough, or turbines in complex terrain where the incoming wind can be inherently heterogeneous. Systematically quantifying the effects of different inflows on the present results, which requires a series of additional simulations, will be carried out in the future work.

The present LES study provides useful insights for developing physics-based engineering wake models. In the literature, dynamic wake meandering model [33] is the most commonly used engineering model for predicting the unsteadiness of turbine power output and dynamic loads. Keck et al. [53] further developed the dynamic wake meandering model to include the effects of shear on wake deficits and incorporated the turbine-added turbulence for turbine arrays. Hahn et al.'s [54] employed a Reynolds-averaged Navier-Stokes (RANS) model to compute the ambient flow in engineering models. Validations of the dynamic wake meandering model can be found in [34, 55, 56]. The dynamic wake meandering model assumes that the wake meandering can be modeled as a passive scalar convected by the incoming turbulent flow. However, the LES results in this work showed that the low frequency, large-scale motion of the wake is dominated by two frequencies, i.e. the low frequency of the inflow, and the frequency of the meandering caused by the wake shear layer instability similar to that of the vortex shedding from bluff bodies [35]. To address this issue, further improvement of the dynamic wake meandering model to account for both the incoming large-scale atmospheric turbulence and the meandering induced by the wake shear layer instability needs to be carried out. In [57], a physics-based engineering model for wind farms of arbitrary size and layout was developed, which can properly model the interaction of the atmospheric turbulent boundary layer with the turbine wakes. However, it cannot take into account the unsteadiness of the incoming atmospheric turbulence and the turbine wakes. Further development of this kind of engineering model, which does not solve the reduced-order equations as in the dynamic wake meandering model, can also be pursued in the future work by adding a model for the large-scale motion of the wake.

One last note is that whether the coordinated axial induction control is effective or not for maximizing the power production of turbine arrays requires further research as there are many other factors, such as the ground roughness, turbine spacing, and etc, affecting the performance of the control strategy. The present work was devoted to provide insights on the fundamental dynamics of turbine wakes although it is motivated by the coordinated axial induction control.

ACKNOWLEDGMENTS

This work was supported by Xcel Energy through the Renewable Development Fund (grant RD4-13). Computational resources were provided by National Renewable Energy Laboratory, the University of Minnesota Supercomputing Institute and the Institute for Advanced Computational Science at the Stony Brook University.

Appendix A: On the calculation of the power spectral density (PSD)

Welch's method [50] is employed for the calculation of the PSD. Let $X(j)$, $j = 0, \dots, N-1$ be the temporal sequence obtained from LES. To compute the PSD, we first divide $X(j)$ into K segments of length L , that

$$X_k(j) = X(j + (k-1)S) \quad j = 0, \dots, L-1, \quad (\text{A1})$$

are the data items in the k^{th} segment, where $k = 0, \dots, K-1$, and S is the separation between two adjacent segments. If the K segments cover the entire sequence, we have $(K-1)S + L = N$ (from which, we can compute K given S , L , and N). We then perform the discrete Fourier transform on the data items in each segment,

$$A_k(n) = \frac{1}{L} \sum_{j=0}^{L-1} X_k(j) W(j) e^{-i2\pi jn/L}, \quad (\text{A2})$$

where $i = \sqrt{-1}$ for each segment, $W(j)$ is a window function. Two window functions were suggested in [50], which are as follows:

$$W_1(j) = 1 - \left| \frac{j - \frac{L-1}{2}}{\frac{L+1}{2}} \right|, \quad j = 0, \dots, L-1, \quad (\text{A3})$$

and

$$W_2(j) = 1 - \left(\frac{j - \frac{L-1}{2}}{\frac{L+1}{2}} \right)^2, \quad j = 0, \dots, L-1. \quad (\text{A4})$$

551 We finally compute the $\text{PSD}(f_n)$ by

$$\text{PSD}(f_n) = \frac{1}{K} \sum_{k=1}^K I_k(f_n), \quad (\text{A5})$$

552 where $f_n = n/L$ (where $n = 0, \dots, L/2$), and $I_k(f_n) = \frac{L}{U} |A_k(n)|^2$ (where $k = 1, \dots, K$, where $U = \frac{1}{L} \sum_{j=0}^{L-1} W^2(j)$).

553 In this appendix, we examine the effects of different window functions and different separations (S) on the computed
 554 PSD. For the present simulation, the number of data points of the entire sequence is $N = 200000$. In all the tests with
 555 different window functions and S , L is fixed at $L = 100000$. Figure 17 shows the effects of different window functions
 556 on the PSD profiles computed at different turbine downwind locations. As seen the differences between the cases with
 557 different window functions are very small especially between W_1 and W_2 . We examine the effects of different values

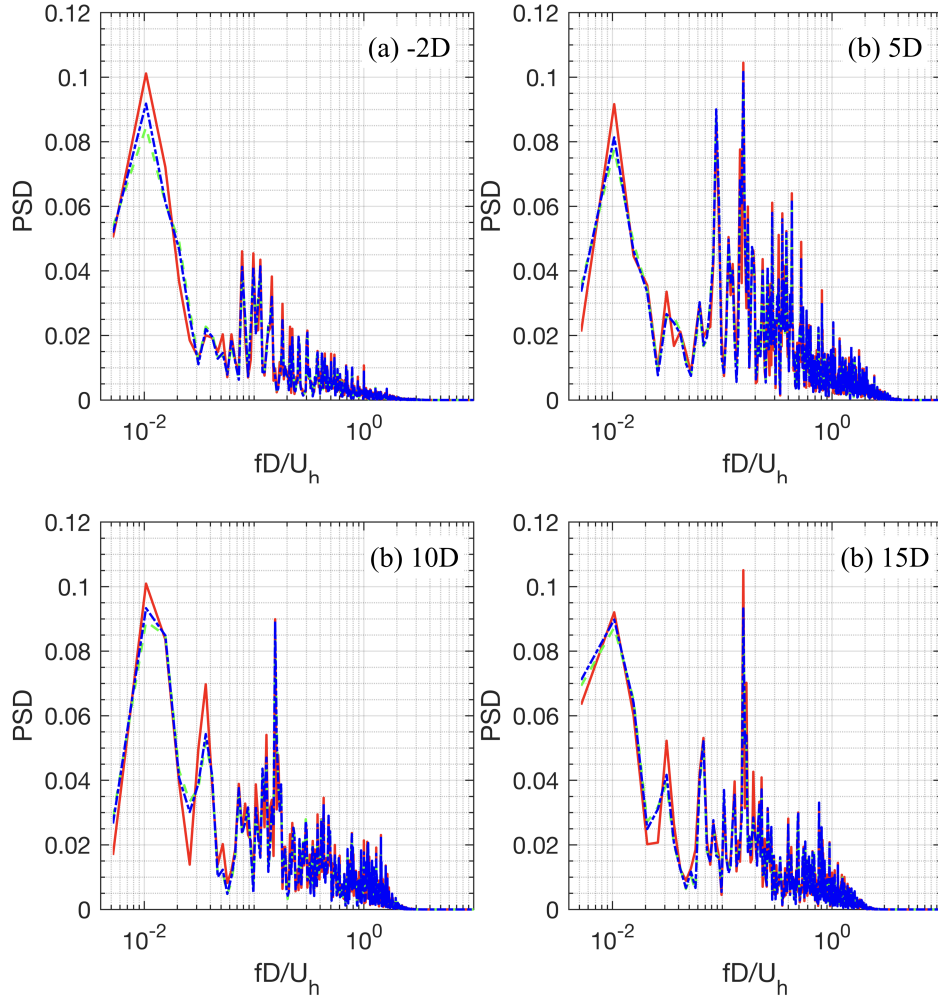


FIG. 17. Effects of different window functions on the PSD profiles at different downwind locations for the $\lambda = 7.8$ case. The PSD is computed using the spanwise velocity fluctuations at different turbine downwind locations along the rotor centerline and normalized by the variance at $x = -2D$. Red solid line: no window function; Green dashed line: W_1 ; Blue dash-dot line: W_2 . The separation between two adjacent segments $S = 2000$

558

559 of separation S on the PSD calculations in figures 18. Four different values of S , i.e. $S = 100000, 50000, 20000$ and
 560 10000 , are tested, which correspond to $K = 2, 3, 6$ and 11 , respectively. Differences between the PSD profiles from
 561 $S = 100000$ and 50000 and those from the other two values of S are observed, while the differences between the PSD
 562 profiles from $S = 20000$ and $S = 10000$ are minor.
 563

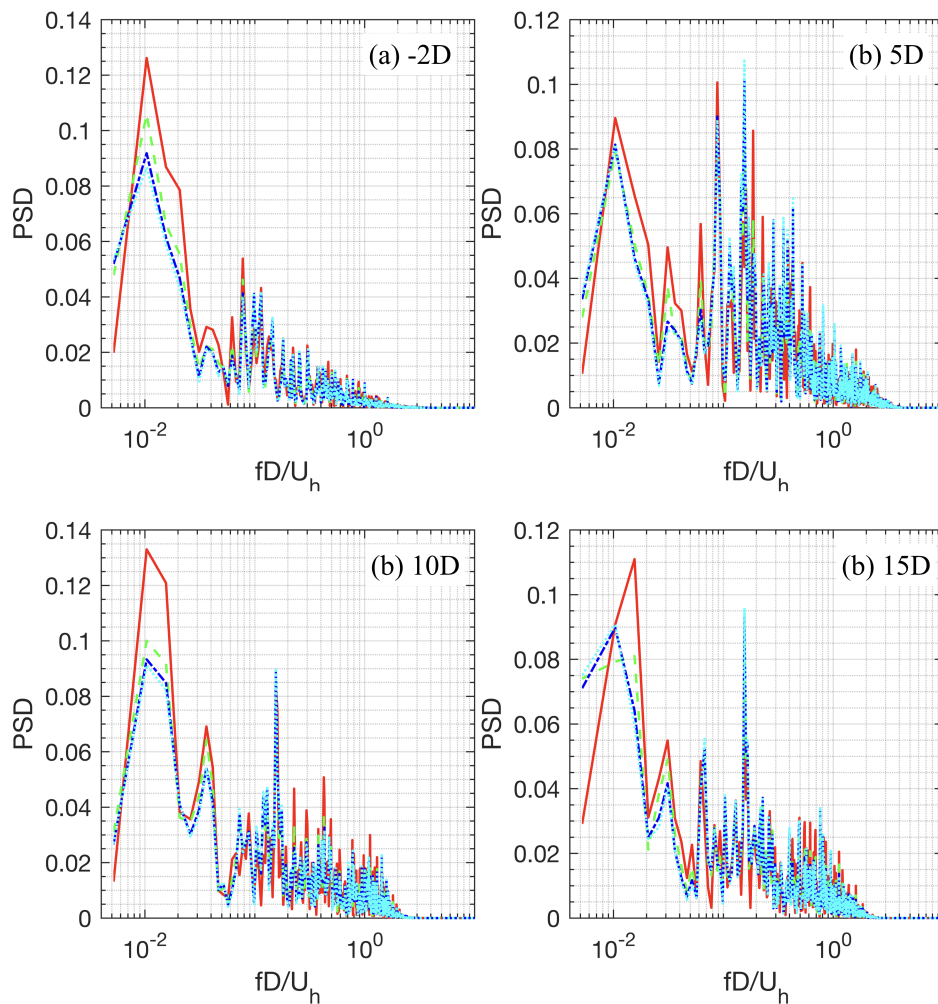


FIG. 18. Effects of different values of separation S on the PSD profiles at different downwind locations for the $\lambda = 7.8$ case. The PSD is computed using the spanwise velocity fluctuations at different turbine downwind locations along the rotor centerline and normalized by the variance at $x = -2D$. Red solid line: $S = 100000$; Green dashed line: $S = 50000$; Blue dash-dot line: $S = 20000$; Cyan dotted line: $S = 10000$. We use $L = 100000$ and the window function W_2 for tests with different values of S .

564

-
- 565 [1] Jay P Goit and Johan Meyers, “Optimal control of energy extraction in wind-farm boundary layers,” *Journal of Fluid*
566 *Mechanics* **768**, 5–50 (2015).
567 [2] Jennifer Annoni, Pieter MO Gebraad, Andrew K Scholbrock, Paul A Fleming, and Jan-Willem van Wingerden, “Analysis
568 of axial-induction-based wind plant control using an engineering and a high-order wind plant model,” *Wind Energy* **19**,
569 1135–1150 (2016).
570 [3] Wim Munters and Johan Meyers, “Dynamic strategies for yaw and induction control of wind farms based on large-eddy
571 simulation and optimization,” *Energies* **11**, 177 (2018).
572 [4] Paul A Fleming, Pieter MO Gebraad, Sang Lee, Jan-Willem van Wingerden, Kathryn Johnson, Matt Churchfield, John
573 Michalakes, Philippe Spalart, and Patrick Moriarty, “Evaluating techniques for redirecting turbine wakes using sowfa,”
574 *Renewable Energy* **70**, 211–218 (2014).
575 [5] Niels Troldborg, Jens N Sorensen, and Robert Mikkelsen, “Numerical simulations of wake characteristics of a wind turbine
576 in uniform inflow,” *Wind Energy* **13**, 86–99 (2010).
577 [6] Wei Tian and Hui Hu, “Effect of oncoming flow turbulence on the kinetic energy transport in the flow around a model
578 wind turbine,” in *2018 Wind Energy Symposium* (2018) p. 0751.

- [7] Leonardo P Chamorro and Fernando Porté-Agel, “A wind-tunnel investigation of wind-turbine wakes: boundary-layer turbulence effects,” *Boundary-layer meteorology* **132**, 129–149 (2009).
- [8] Leonardo P Chamorro and Fernando Porté-Agel, “Effects of thermal stability and incoming boundary-layer flow characteristics on wind-turbine wakes: a wind-tunnel study,” *Boundary-layer meteorology* **136**, 515–533 (2010).
- [9] Wei Zhang, Corey D Markfort, and Fernando Porté-Agel, “Wind-turbine wakes in a convective boundary layer: a wind-tunnel study,” *Boundary-layer meteorology* **146**, 161–179 (2013).
- [10] KB Howard, JS Hu, LP Chamorro, and M Guala, “Characterizing the response of a wind turbine model under complex inflow conditions,” *Wind Energy* **18**, 729–743 (2015).
- [11] LP Chamorro, C Hill, VS Neary, B Gunawan, REA Arndt, and F Sotiropoulos, “Effects of energetic coherent motions on the power and wake of an axial-flow turbine,” *Physics of Fluids* **27**, 055104 (2015).
- [12] M Maureen Hand, Neil D Kelley, and Mark J Balas, “Identification of wind turbine response to turbulent inflow structures,” in *ASME/JSME 2003 4th Joint Fluids Summer Engineering Conference* (American Society of Mechanical Engineers, 2003) pp. 2557–2566.
- [13] Ferhat Bingöl, Jakob Mann, and Gunner C Larsen, “Light detection and ranging measurements of wake dynamics part i: one-dimensional scanning,” *Wind energy* **13**, 51–61 (2010).
- [14] Juan-José Trujillo, Ferhat Bingöl, Gunner C Larsen, Jakob Mann, and Martin Kühn, “Light detection and ranging measurements of wake dynamics. part ii: two-dimensional scanning,” *Wind Energy* **14**, 61–75 (2011).
- [15] Said El-Asha, Lu Zhan, and Giacomo Valerio Iungo, “Quantification of power losses due to wind turbine wake interactions through scada, meteorological and wind lidar data,” *Wind Energy* **20**, 1823–1839 (2017).
- [16] Xiaolei Yang, Fotis Sotiropoulos, Robert J Conzemius, John N Wachtler, and Mike B Strong, “Large-eddy simulation of turbulent flow past wind turbines/farms: the virtual wind simulator (VWiS),” *Wind Energy* **18**, 2025–2045 (2015).
- [17] Daniel Foti, Xiaolei Yang, Filippo Campagnolo, David Maniaci, and Fotis Sotiropoulos, “On the use of spires for generating inflow conditions with energetic coherent structures in large eddy simulation,” *Journal of Turbulence* **18**, 611–633 (2017).
- [18] Francesco Viola, Giacomo Valerio Iungo, Simone Camarri, Fernando Porté-Agel, and Francois Gallaire, “Prediction of the hub vortex instability in a wind turbine wake: stability analysis with eddy-viscosity models calibrated on wind tunnel data,” *Journal of Fluid Mechanics* **750**, R1 (2014).
- [19] Kevin B Howard, Arvind Singh, Fotis Sotiropoulos, and Michele Guala, “On the statistics of wind turbine wake meandering: An experimental investigation,” *Physics of Fluids (1994-present)* **27**, 075103 (2015).
- [20] Luis A Martínez Tossas, Richard JAM Stevens, and Charles Meneveau, “Wind turbine large-eddy simulations on very coarse grid resolutions using an actuator line model,” *34th Wind Energy Symposium, AIAA SciTech*, AIAA 2016–1261 (2016).
- [21] Daniel Foti, Xiaolei Yang, Michele Guala, and Fotis Sotiropoulos, “Wake meandering statistics of a model wind turbine: Insights gained by large eddy simulations,” *Physical Review Fluids* **1**, 044407 (2016).
- [22] Seokkoo Kang, Xiaolei Yang, and Fotis Sotiropoulos, “On the onset of wake meandering for an axial flow turbine in a turbulent open channel flow,” *Journal of Fluid Mechanics* **744**, 376–403 (2014).
- [23] Christian Santoni, Kenneth Carrasquillo, Isnardo Arenas-Navarro, and Stefano Leonardi, “Effect of tower and nacelle on the flow past a wind turbine,” *Wind Energy* **20**, 1927–1939 (2017).
- [24] Christian Santoni, Umberto Ciri, Mario Rotea, and Stefano Leonardi, “Development of a high fidelity cfd code for wind farm control,” in *American Control Conference (ACC), 2015* (IEEE, 2015) pp. 1715–1720.
- [25] Xiaolei Yang and Fotis Sotiropoulos, “A new class of actuator surface models for wind turbines,” *Wind Energy* **21**, 285–302 (2018).
- [26] Jiarong Hong, Mostafa Toloui, Leonardo P Chamorro, Michele Guala, Kevin Howard, Sean Riley, James Tucker, and Fotis Sotiropoulos, “Natural snowfall reveals large-scale flow structures in the wake of a 2.5-mw wind turbine,” *Nature communications* **5**, 4216 (2014).
- [27] Leonardo P Chamorro, S-J Lee, D Olsen, C Milliren, J Marr, REA Arndt, and F Sotiropoulos, “Turbulence effects on a full-scale 2.5 mw horizontal-axis wind turbine under neutrally stratified conditions,” *Wind Energy* **18**, 339–349 (2015).
- [28] Kevin B Howard and Michele Guala, “Upwind preview to a horizontal axis wind turbine: a wind tunnel and field-scale study,” *Wind Energy* **19**, 1371–1389 (2016).
- [29] Xiaolei Yang, Jennifer Annoni, Pete Seiler, and Fotis Sotiropoulos, “Modeling the effect of control on the wake of a utility-scale turbine via large-eddy simulation,” in *Journal of Physics: Conference Series*, Vol. 524 (IOP Publishing, 2014) p. 012180.
- [30] Xiaolei Yang, Jiarong Hong, Matthew Barone, and Fotis Sotiropoulos, “Coherent dynamics in the rotor tip shear layer of utility-scale wind turbines,” *Journal of Fluid Mechanics* **804**, 90–115 (2016).
- [31] Daniel Foti, Xiaolei Yang, and Fotis Sotiropoulos, “Similarity of wake meandering for different wind turbine designs for different scales,” *Journal of Fluid Mechanics* **842**, 5–25 (2018).
- [32] Xiaolei Yang, Kevin B Howard, Michele Guala, and Fotis Sotiropoulos, “Effects of a three-dimensional hill on the wake characteristics of a model wind turbine,” *Physics of Fluids* **27**, 025103 (2015).
- [33] Gunner C Larsen, Helge Aa Madsen, Ferhat Bingöl, Jakob Mann, Søren Ott, Jens N Sørensen, Valery Okulov, Niels Troldborg, Morten Nielsen, Kenneth Thomsen, *et al.*, “Dynamic wake meandering modeling,” *Risø National Laboratory, Technical University of Denmark, Roskilde, Denmark, Risø* (2007).
- [34] Torben J Larsen, Helge Aa Madsen, Gunner C Larsen, and Kurt S Hansen, “Validation of the dynamic wake meander model for loads and power production in the egmond aan zee wind farm,” *Wind Energy* **16**, 605–624 (2013).
- [35] Davide Medici and PH Alfredsson, “Measurements on a wind turbine wake: 3d effects and bluff body vortex shedding,” *Wind Energy* **9**, 219–236 (2006).

- 643 [36] D Medici and P Henrik Alfredsson, “Measurements behind model wind turbines: further evidence of wake meandering,”
644 *Wind Energy* **11**, 211–217 (2008).
- 645 [37] Daniel Foti, Xiaolei Yang, Filippo Campagnolo, David Maniaci, and Fotis Sotiropoulos, “On the wake meandering of a model
646 wind turbine operating in two different regimes,” Submitted to *Physical Review: Fluids*, arXiv:1802.03836 [physics.flu-dyn]
647 (2018).
- 648 [38] Antoni Calderer, Xiaolei Yang, Dionysios Angelidis, Ali Khosronejad, Trung Le, Seokkoo Kang, Anvar Gilmanov, Liang
649 Ge, and Iman Borazjani, *Virtual Flow Simulator*, Tech. Rep. (University of Minnesota, 2015).
- 650 [39] Antoni Calderer, Xin Guo, Lian Shen, and Fotis Sotiropoulos, “Fluid–structure interaction simulation of floating structures
651 interacting with complex, large-scale ocean waves and atmospheric turbulence with application to floating offshore wind
652 turbines,” *Journal of Computational Physics* **355**, 144–175 (2018).
- 653 [40] Xiaolei Yang, Maggie Pakula, and Fotis Sotiropoulos, “Large-eddy simulation of a utility-scale wind farm in complex
654 terrain,” *Applied Energy* **229**, 767–777 (2018).
- 655 [41] Massimo Germano, Ugo Piomelli, Parviz Moin, and William H Cabot, “A dynamic subgrid-scale eddy viscosity model,”
656 *Physics of Fluids A: Fluid Dynamics (1989-1993)* **3**, 1760–1765 (1991).
- 657 [42] Liang Ge and Fotis Sotiropoulos, “A numerical method for solving the 3d unsteady incompressible navier–stokes equations
658 in curvilinear domains with complex immersed boundaries,” *Journal of computational physics* **225**, 1782–1809 (2007).
- 659 [43] Xiaolei Yang, Xing Zhang, Zhilin Li, and Guo-Wei He, “A smoothing technique for discrete delta functions with application
660 to immersed boundary method in moving boundary simulations,” *Journal of Computational Physics* **228**, 7821–7836 (2009).
- 661 [44] Zhaohui Du and Michael S Selig, “A 3-D stall-delay model for horizontal axis wind turbine performance prediction,” *AIAA*
662 *Paper* **21** (1998).
- 663 [45] Wen Zhong Shen, Jens Nørkær Sørensen, and Robert Mikkelsen, “Tip loss correction for actuator/navier–stokes compu-
664 tations,” *Journal of Solar Energy Engineering* **127**, 209–213 (2005).
- 665 [46] Wen Zhong Shen, Robert Mikkelsen, Jens Nørkær Sørensen, and Christian Bak, “Tip loss corrections for wind turbine
666 computations,” *Wind Energy* **8**, 457–475 (2005).
- 667 [47] Herrmann Schlichting and Klaus Gersten, *Boundary-layer theory* (Springer Science & Business Media, 2003).
- 668 [48] Di Yang, Charles Meneveau, and Lian Shen, “Effect of downwind swells on offshore wind energy harvesting—a large-eddy
669 simulation study,” *Renewable Energy* **70**, 11–23 (2014).
- 670 [49] Daniel Foti, Xiaolei Yang, Filippo Campagnolo, David Maniaci, and Fotis Sotiropoulos, “Wake meandering of a model
671 wind turbine operating in two different regimes,” *Physical Review Fluids* **3**, 054607 (2018).
- 672 [50] Peter Welch, “The use of fast fourier transform for the estimation of power spectra: a method based on time averaging
673 over short, modified periodograms,” *IEEE Transactions on audio and electroacoustics* **15**, 70–73 (1967).
- 674 [51] Ewan Machefaux, Gunner Chr Larsen, and Jakob Mann, *Multiple Turbine Wakes* (DTU Wind Energy, 2015).
- 675 [52] Michael Heisel, Jiarong Hong, and Michele Guala, “The spectral signature of wind turbine wake meandering: A wind
676 tunnel and field-scale study,” *Wind Energy* (2018).
- 677 [53] Rolf-Erik Keck, Martin de Maré, Matthew J Churchfield, Sang Lee, Gunner Larsen, and Helge Aagaard Madsen, “Two
678 improvements to the dynamic wake meandering model: including the effects of atmospheric shear on wake turbulence and
679 incorporating turbulence build-up in a row of wind turbines,” *Wind Energy* **18**, 111–132 (2015).
- 680 [54] S Hahn, E Machefaux, YV Hristov, M Albano, and R Threadgill, “Estimation of annual energy production using dynamic
681 wake meandering in combination with ambient cfd solutions,” in *Journal of Physics: Conference Series*, Vol. 753 (IOP
682 Publishing, 2016) p. 032043.
- 683 [55] Matthew J Churchfield, Sang Lee, Patrick J Moriarty, Yujia Hao, Matthew A Lackner, Rebecca Barthelmie, Julie K
684 Lundquist, and Gregory Oxley, “A comparison of the dynamic wake meandering model, large-eddy simulation, and field
685 data at the egmond aan zee offshore wind plant,” in *33rd Wind Energy Symposium* (2015) p. 0724.
- 686 [56] Torben J Larsen, Gunner Chr Larsen, Mads Mølgaard Pedersen, Karen Enevoldsen, and HA Madsen, “Validation of
687 the dynamic wake meander model with focus on tower loads,” in *Journal of Physics: Conference Series*, Vol. 854 (IOP
688 Publishing, 2017) p. 012027.
- 689 [57] Xiaolei Yang and Fotis Sotiropoulos, “Analytical model for predicting the performance of arbitrary size and layout wind
690 farms,” *Wind Energy* **19**, 1239–1248 (2016).